

HIGH RESOLUTION RADIO AND OPTICAL OBSERVATIONS OF THE CENTRAL STARBURST IN THE LOW-METALLICITY DWARF GALAXY II ZW 40

AMANDA A. KEPLEY¹

Department of Astronomy, University of Virginia, P.O. Box 400325, Charlottesville, VA 22904-4325, USA

AMY E. REINES²

Department of Astronomy, University of Virginia, P.O. Box 400325, Charlottesville, VA 22904-4325, USA; and National Radio
Astronomy Observatory, 520 Edgemont Road, Charlottesville, VA 22903, USA

KELSEY E. JOHNSON, LISA MAY WALKER

Department of Astronomy, University of Virginia, P.O. Box 400325, Charlottesville, VA 22904-4325, USA

Draft version January 24, 2021

ABSTRACT

The extent to which star formation varies in galaxies with low masses, low metallicities, and high star formation rate surface densities is not well-constrained. To gain insight into star formation under these physical conditions, this paper estimates the ionizing photon fluxes, masses, and ages for young massive clusters in the central region of II Zw 40 – the prototypical low-metallicity dwarf starburst galaxy – from radio continuum and optical observations. Discrete, cluster-sized sources only account for half the total radio continuum emission; the remainder is diffuse. The young ($\lesssim 5$ Myr) central burst has a star formation rate surface density that significantly exceeds that of the Milky Way. Three of the 13 sources have ionizing photon fluxes (and thus masses) greater than R136 in 30 Doradus. Although isolating the effects of galaxy mass and metallicity is difficult, the H II region luminosity function and the internal extinction in the center of II Zw 40 appear to be primarily driven by a merger-related starburst. The relatively flat H II region luminosity function may be the result of an increase in ISM pressure during the merger and the internal extinction is similar to that generated by the clumpy and porous dust in other starburst galaxies.

Subject headings: Galaxies: individual (II Zw 40), Galaxies: ISM, Galaxies: starburst, Galaxies: star formation, Galaxies: star clusters: general, Radio continuum: galaxies

1. INTRODUCTION

Dwarf starburst galaxies have the potential to provide vital information about how star formation proceeds when subject to physical conditions not present in the Milky Way. These galaxies typically have lower masses, lower metallicities, and much higher star formation rate surface densities than spiral galaxies, which may change what physical processes are important for star formation and the properties of the stars and clusters in the galaxy.

The effects of the unique environment for star formation found in dwarf starburst galaxies can manifest in several ways. First, the clusters in these galaxies may be larger than the clusters in normal galaxies due to either lack of large-scale shear from differential rotation (Weidner et al. 2010), higher gas pressures (Elmegreen & Efremov 1997), or high gas densities decreasing the effectiveness of radiation pressure for fragmenting molecular clouds (Krumholz et al. 2010). Second, the molecular gas tracers in these galaxies may have different properties than the molecular gas tracers in more normal galaxies: there are fewer metals overall, less dust to serve as a formation site for molecular

hydrogen, and the harder radiation fields may destroy more dust (Galliano et al. 2003, 2005; Madden et al. 2006) and molecules (e.g. Bolatto et al. 2008). Finally, star formation may be regulated by different mechanisms in dwarf starburst galaxies including the radiation pressure and/or H II region expansion (Murray et al. 2010) and the injection of turbulence by supernovae (Ostriker & Shetty 2011).

The prototypical dwarf starburst galaxy II Zw 40 provides an important test case for models of star formation in low-mass, low-metallicity, and high star formation rate surface density environments. This galaxy, along with I Zw 18, originally defined the blue compact dwarf galaxy class, which consists primarily of low mass, low metallicity, starbursting galaxies (Sargent & Searle 1970; Searle & Sargent 1972; see Gil de Paz et al. (2003) for an updated definition). The total dynamic mass of II Zw 40 ($6 \times 10^9 M_{\odot}$; Brinks & Klein 1988) is only 4% of the total dynamic mass of the Milky Way. Furthermore, II Zw 40 has a metallicity of only $1/5 Z_{\odot}$ ($12 + \log(\text{O}/\text{H}) = 8.09$; Guseva et al. 2000). Finally, the star formation rate surface density for this entire dwarf galaxy is $0.4 M_{\odot} \text{ yr}^{-2} \text{ kpc}^{-2}$, which is comparable to other starburst galaxies (cf. Figure 15 in Bigiel et al. 2008).

Even in low-metallicity environments, young star-forming regions can still be subject to significant internal extinction, making them difficult to study in the opti-

akepley@nrao.edu

areines@nrao.edu

kej7a@virginia.edu, lisamay@virginia.edu

¹ currently at the National Radio Astronomy Observatory,
P.O. Box 2, Green Bank, WV 24944, USA

² Einstein Fellow

cal and infrared (Thuan et al. 1999; Plante & Sauvage 2002; Galliano et al. 2003, 2005). In the radio, however, free-free emission from the ionized gas surrounding young massive stars is minimally affected by extinction by dust. Consequently, free-free emission provides us with an important tool for inferring the properties of the young massive clusters that may be partially or totally obscured at optical wavelengths. It is not perfect tool though: the number of ionizing photons produced by the obscured, young, massive stars may be underestimated because these photons are absorbed by dust or escape from the region (see the discussion in Section 3.1.3).

The goal of this paper is to quantify the properties of star formation in the low-metallicity, low-mass, and high star formation rate surface density environment found in II Zw 40. We present measurements of the young massive cluster population in II Zw 40 using new 6.2 cm, 3.5 cm, and 1.3 cm radio continuum images from the National Radio Astronomy Observatory (NRAO) Very Large Array (VLA)³ (§ 2.1) and previously unpublished high-resolution optical F555W (\sim V-band), F658N (H α), and F814W (\sim I-band) images from the Advanced Camera for Surveys (ACS) on the *Hubble Space Telescope* (HST)⁴ (§ 2.2). We describe the properties of the young massive clusters as seen in the radio continuum (§ 3.1) and the optical (§ 3.2). Then we discuss the implications of our results including the cluster luminosity function as traced by the H II region luminosity function (§ 4.1) and the internal dust extinction (§ 4.2). Finally, we summarize our results and present our conclusions and their implications (§ 5).

This paper assumes a distance to II Zw 40 of 10 Mpc (Tully & Fisher 1988). At this distance, 0.1'' corresponds to 4.8 pc.

2. DATA

To trace the obscured young massive star formation in II Zw 40, we obtained high resolution radio continuum observations at 6.2 cm, 3.5 cm, and 1.3 cm with the VLA. The array configurations were chosen to produce relatively matched u - v coverage at each frequency. These new observations have the sensitivity and resolution necessary to probe the physical scales and flux densities of embedded star forming regions; they are 2.4 to 7 times more sensitive in surface brightness, 4 to 20 times deeper in point source sensitivity, and 2 to 3 times higher resolution than the previous highest resolution radio continuum survey (Beck et al. 2002).⁵ Table 1 summarizes the radio continuum data used in this paper. The calibration and imaging of these data are detailed in § 2.1

To obtain a more complete picture of star formation in II Zw 40, this paper also includes high resolution optical F555W (similar to V-band), F658N (H α), and F814W

(similar to I-band) observations from the *HST*. We use these data to parameterize the unobscured young massive clusters in II Zw 40 – in particular, the two bright optically visible SSCs. The optical data also measure the H α emission from the ionized gas. More detailed information on the *HST* data is provided in § 2.2.

Figure 1 gives an overview of the observations presented here, illustrating the overall morphology and size of II Zw 40 and the central few hundred parsec region of II Zw 40 probed by our observations.

2.1. VLA Data

The details for the VLA observations are given in Table 1. The use of the Pie Town link, a Very Long Baseline Array (VLBA) antenna located approximately 52 km away from the main VLA site, doubles the resolution of the VLA A configuration (Ulvestad et al. 1998). For all the observations, the correlator was set up to provide two 50 MHz IFs. These IFs were tuned to 4.8851 and 4.8351 GHz, 8.4351 GHz and 8.4851 GHz, and 22.4851 and 22.4351 GHz for the 6.2 cm, 3.5 cm, and 1.3 cm observations, respectively. For the 1.3 cm observations, reference pointing was done every hour to minimize pointing errors and fast switching mode was used to minimize atmospheric phase variations. We have removed the 4 EVLA antennas from the August 2006 data set to avoid introducing phase closure errors in the crossed (EVLA-VLA) baselines because of mismatches in the bandpasses of the VLA and EVLA receivers.

The 6.2 cm and 3.5 cm data were reduced using the standard AIPS reduction procedures detailed in Appendix A of the AIPS Cookbook (Greisen 2010). Here we provide a sketch of the calibration. The data were read in with FILLM and the flux density of the primary calibrator was established using SETJY. Then the amplitude and phases of the primary and secondary calibrator were determined using CALIB; a model was used for the primary calibrator and the secondary calibrator was assumed to be a point source. The flux density of the secondary calibrators were determined using GETJY. Finally, the calibration solutions were applied using CLCAL.

The 1.3 cm data were reduced following the procedure in Appendix D in the AIPS Cookbook (Greisen 2010). First, the data were read in and had atmospheric corrections applied based on current and seasonal weather data using the task FILLM. The positions of the antennas were corrected using the task VLANT. Then, we set the flux density of the primary calibrator using SETJY. We calibrated the phases of the primary and secondary calibrators with CALIB using a solution interval of 30s, again using a model for the primary calibrator and assuming the secondary calibrator is a point source. For the August 2006 observations, the u - v range for the solutions for the secondary calibrator was restricted to baselines less than 300 k λ . The other data sets were taken during better conditions and the u - v range of the solutions did not need to be restricted to produce a good calibration. We applied these phase calibrations using CLCAL. Then we calibrated the amplitudes and phases of the primary and secondary calibrators with CALIB using the scan length as the solution interval. Again, for the August 2006 data set we restricted the solution for the secondary calibrators to baselines to less than 300

³ The National Radio Astronomy Observatory is a facility of the National Science Foundation operated under cooperative agreement by Associated Universities, Inc.

⁴ Based on observations made with the NASA/ESA Hubble Space Telescope, obtained from the Data Archive at the Space Telescope Science Institute, which is operated by the Association of Universities for Research in Astronomy, Inc., under NASA contract NAS 5-26555. These observations are associated with program #6739.

⁵ We included some of the archival data from Beck et al. (2002) to increase sensitivity and avoid unnecessarily duplicating observations.

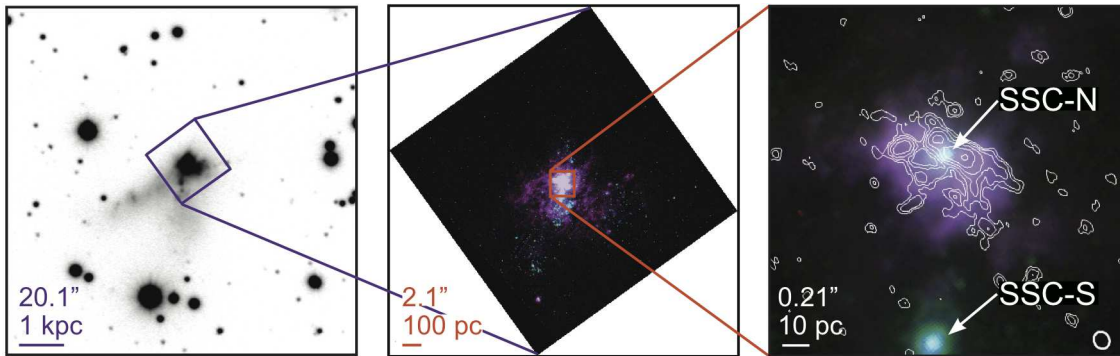


FIG. 1.— *Left*: R band image of II Zw 40 from Gil de Paz et al. (2003). The two linear features extending to the east and south are suggestive of tidal tails. *Middle*: *HST* ACS image of II Zw 40 from archival observations by R. Chandar. Blue represents the F555W filter (V-band), green represents the F814W filter (I-band), and red represents the F658N filter ($H\alpha$). Note the extended diffuse $H\alpha$ component throughout the central region of the galaxy. *Right*: Contours from our 1.3 cm robust = 0 image overlaid on the central region of the ACS image with the same color scheme as in the middle panel. The contours start at the 3σ noise level for the 1.3 cm robust = 0 image and increase by factors of $2^{n/2}$, where $n = 1, 2, 3, \dots$. The beam for the 1.3 cm robust = 0 image is given in the lower right hand corner of the image. The two optical sources (SSC-N and SSC-S) are discussed in § 3.2.

$k\lambda$. We bootstrapped the flux density of the secondary calibrators from the flux density of the primary calibrator using GETJY. Finally, we applied the antenna-based amplitude and phase calibration using CLCAL.

The process of creating images from the visibilities measured by an interferometer depends on the scientific goals of the project and the properties of the data. Our two goals for this data – to measure the radio continuum spectrum and to identify individual radio continuum sources – required us to produce two different sets of images.

To measure the global radio continuum spectrum, we matched the spatial resolutions and u - v coverage at different wavelengths to reduce systematic effects from differences in spatial sampling. The matched u - v coverage 6.2 cm, 3.5 cm, and 1.3 cm images are shown on the same spatial scale in Figure 2 and image properties are given in Table 2. We note that cleaning the images does not change the derived total flux. The total flux in an image with a zero-spacing flux value of 18 mJy (the Klein et al. 1991 value for the total 22 GHz flux) is within 0.2% of the total flux in an image with zero-spacing flux value of 0 mJy.

The spatial resolution of the matched beam images is 12 to 20 pc: too large to probe the physical size scales of natal clusters. To identify and measure the properties of individual radio continuum sources, we produced a high resolution, robust=0 image of the 1.3 cm continuum data with a physical resolution of 6.7 by 5.8 pc: two to three times higher than the resolution of the matched images and comparable to the size scales of individual clusters. The 1.3 cm robust = 0 image is shown in Figure 3 and the image properties are given in Table 2.

2.2. *HST* ACS data

HST observations of II Zw 40 were obtained with the ACS High Resolution Channel (HRC) on 2003 November 26 (*HST* proposal 6739, PI: R. Chandar). Images were taken with the F555W, F658N, and F814W filters. We retrieved the pipeline-produced calibrated and drizzled images from the archive. The HRC plate scale is $\sim 0''.025$ pixel $^{-1}$ and the images have a resolution of $\sim 0''.075$.

The F555W and F814W filters are broad and can be contaminated by nebular emission from young ($\lesssim 5$ Myr)

clusters (Reines et al. 2010). In addition, at the redshift of II Zw 40, the F658N narrow-band filter contains both the $H\alpha$ and $[\text{NII}]\lambda 6584$ emission lines. However, spectroscopic observations of the brightest part of the galaxy show that the $[\text{NII}]\lambda 6584$ flux density is only $\sim 2\%$ of the $H\alpha$ flux density (Guseva et al. 2000). Therefore, we expect the contamination from this line to be negligible.

The nominal astrometry of the *HST*/ACS images is only accurate to within $\sim 1''$ while the VLA astrometry is good to within $\sim 0''.1$ and is considered absolute by comparison. We therefore register the optical *HST* images to the high resolution VLA 1.3 cm image by bootstrapping from a continuum-subtracted *HST* NICMOS Paschen α image which traces the same ionized gas as the thermal radio emission (modulo extinction). The F658N ACS image containing both $H\alpha$ emission and stellar continuum was then registered to the Paschen α image. The F555W and F814W ACS images are aligned with the registered F658N image. We estimate that the final relative astrometry is accurate to $\lesssim 0''.1$ based on a comparison of the Paschen α data and the radio continuum data.

Figure 3 shows the distribution of the re-registered *HST* ACS F658N, F555W, and F814W and the NICMOS Paschen α compared to our highest resolution 1.3 cm data.

3. RESULTS

3.1. Properties of the Radio Continuum Emission

Here we describe the measured properties of the radio continuum emission in II Zw 40 and quantify the young, still obscured, massive cluster population in this galaxy. We start by using the radio continuum emission spectrum of the central region of II Zw 40 to determine whether the radio continuum emission there is predominantly thermal free-free emission produced by young massive clusters or non-thermal synchrotron emission produced by supernovae (§3.1.1). We then identify discrete radio continuum sources and measure their flux densities (§ 3.1.2). Finally, we estimate the physical properties of the sources (§ 3.1.3).

3.1.1. Radio Continuum Spectrum

The radio continuum spectrum reveals the dominant emission mechanisms in a region. In general, the radio

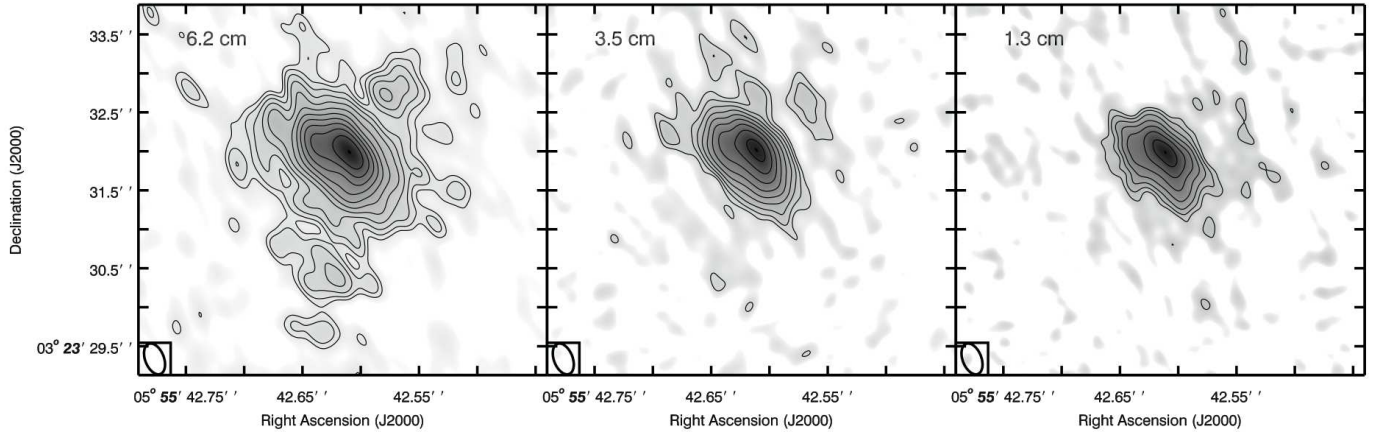


FIG. 2.— Matched $u-v$ coverage images of our data at 6.2 cm (*left*), 3.5 cm (*middle*), and 1.3 cm (*right*). The contours start at the 3σ noise level for each image and increase by factors of $2^{n/2}$, where $n = 1, 2, 3, \dots$. The beam is shown in the lower left hand corner of each panel.

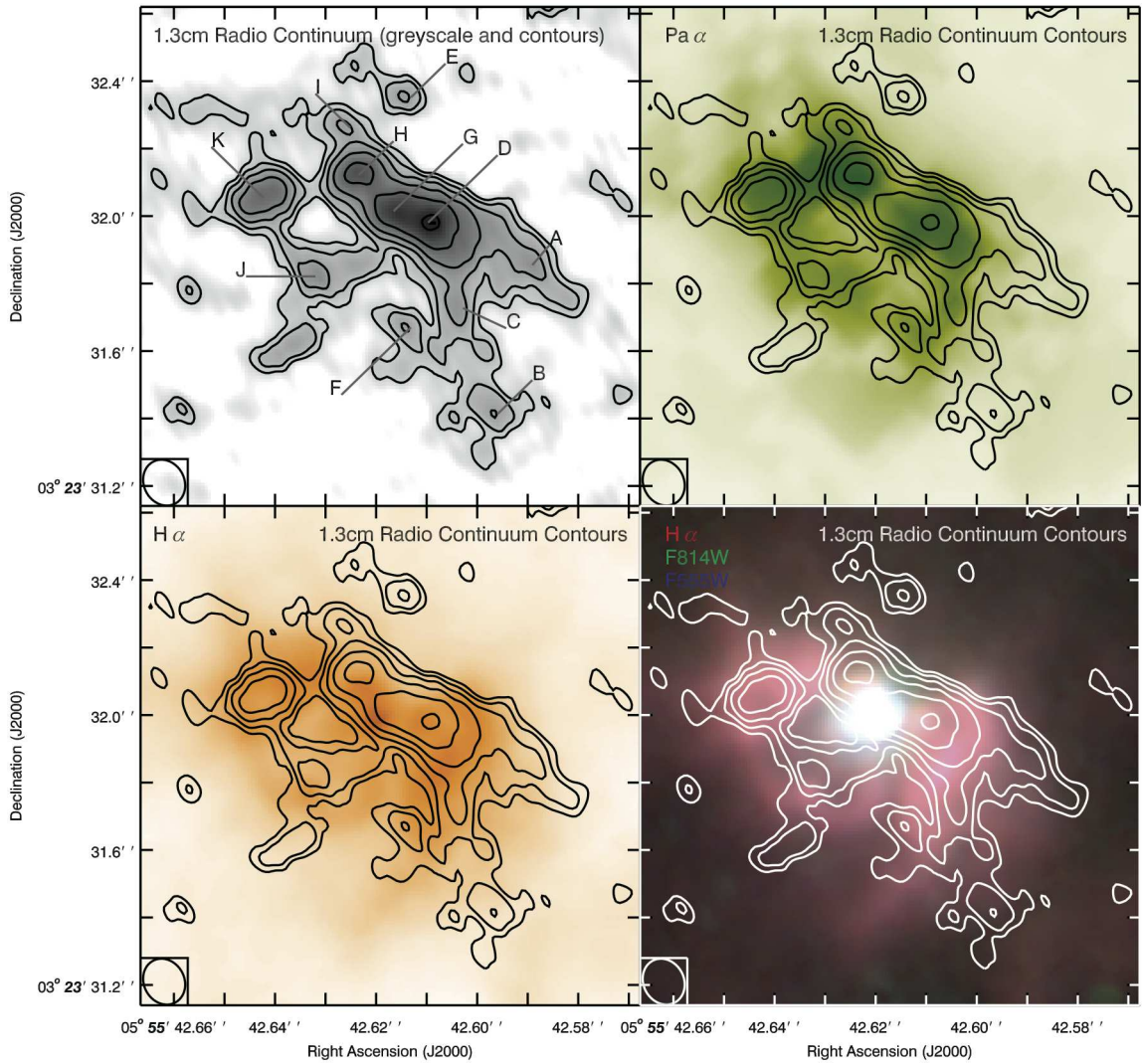


FIG. 3.— *Top Left:* Zoomed in version of 1.3 cm robust = 0 image. The contours start at the 3σ noise level and increase by factors of $2^{n/2}$, where $n = 1, 2, 3, \dots$. The beam is shown in the lower left hand corner. The same contours and beam are shown in the other three panels. The letters indicate the sources identified in Section 3.1.2 and are ordered by increasing RA. *Top Right:* Continuum subtracted NICMOS Paschen α image of II Zw 40. *Bottom Left:* The F658N ACS image, which corresponds to H α , of II Zw 40. The F658N image is not continuum subtracted. *Bottom Right:* Three color optical image of II Zw 40. In this image, blue is used for the ACS F555W filter image (roughly V-band), green is used for the F814W filter image (roughly I-band), and red is used for the ACS F658N image (H α).

continuum spectrum consists of two components: a thermal component generated by free-free emission and associated with young massive clusters and a non-thermal component generated by synchrotron emission and associated with supernovae. To first order, the intrinsic spectra of the optically thin free-free emission and synchrotron emission can both be represented by power laws with spectral indices⁶ of -0.1 and ≈ -0.7 , respectively. The spectral index of the free-free emission is well-defined, but the spectral index of the synchrotron emission has a large variation because it depends on the cosmic ray electron spectrum (Beck & Krause 2005).

We measured the radio continuum spectrum of the central region of II Zw 40 to determine the main emission mechanisms at work (Table 4). The flux densities at each frequency were determined using an aperture $6''$ in diameter; this aperture includes the entire central emission region at all three frequencies. We estimate that the flux density errors are 20%. This error takes into account the typical uncertainty in absolute flux density calibration for the VLA ($\lesssim 3\%$; Perley & Butler 2012) and the uncertainty in the photometry derived from a comparison of different photometry methods (Gaussian fitting, SURPHOT (see § 3.1.2), CASA⁷ image viewer regions).

The matched u - v coverage images are not sensitive to emission on scales larger than $18.4''$ due to the inner 11.2 k λ cut-off in u - v space and thus may underestimate the total amount of flux in the region. We use the radio continuum spectrum model from Klein et al. (1991) to estimate the amount of missing flux in our images. This model is based on single-dish data and interferometer measurements that are sensitive to much larger angular scales than our data. Comparing our data with this model shows that our matched u - v coverage images do not include approximately 50-60% of total radio continuum flux (Table 4). Therefore, the radio continuum spectrum that we derive is specific to the compact central region of II Zw 40 rather than the entire galaxy and represents only the emission with spatial frequencies between 11.2 and 1000 k λ .

Since there are flux density measurements at only three frequencies, the most appropriate model for the data is the following (Duric et al. 1988; Niklas et al. 1997):

$$\frac{S}{S_0} = p_{th} \left(\frac{\nu}{\nu_0}\right)^{-0.1} + (1 - p_{th}) \left(\frac{\nu}{\nu_0}\right)^{\alpha_{nt}} \quad (1)$$

where S is the flux density at frequency ν , S_0 is the flux density at frequency ν_0 , p_{th} is the fraction of thermal emission, and α_{nt} is the spectral index of the non-thermal emission.

The radio continuum spectrum for the central region of II Zw 40 appears to be dominated by thermal emission with a smaller non-thermal component (Figure 4). The 1.3 cm and 3.5 cm points can be fit by a single power law with a spectral index of -0.1 . Adding the 6.2 cm data point requires including a non-thermal component. This non-thermal component contributes approximately 20% of the total flux density at 6.2 cm. Using the calculated χ^2 values for a range of p_{th} and α_{nt} values, the best fit values for p_{th} and α_{nt} are 0.99 and -2.17 with

a reduced chi-squared value of 0.0065 (bottom panel of Figure 4). The best reduced chi-squared value is significantly lower than 1.0 , suggesting that the errors on our data may be overly conservative. However, we retain the larger 20% errors because they better reflect the systematic uncertainties in our data, not just the much smaller measurement errors. The value for p_{th} is well determined and lies between 0.75 and 1.0 . The value of α_{nt} is much less well determined and ranges from -0.5 to -2.17 . The latter value is unrealistically steep for α_{nt} , so we interpret this constraint as $\alpha_{nt} \leq -0.5$. These results are consistent with previous studies of II Zw 40 (Sramek & Weedman 1986; Klein et al. 1991; Deeg et al. 1993; Beck et al. 2002), although the spectrum measured here is specific to the spatial scales included in our images and is not representative of the total radio continuum spectrum of II Zw 40 because of the missing large-scale flux.

The weak synchrotron emission in the central region of II Zw 40 implies its current supernova rate is low. In our Galaxy, the synchrotron luminosity is related to the supernova rate by

$$\left(\frac{L_N}{10^{22} \text{W Hz}^{-1}}\right) \sim 13 \left(\frac{\nu}{\text{GHz}}\right)^{\alpha_{nt}} \left(\frac{\nu_{sn}}{\text{yr}^{-1}}\right) \quad (2)$$

where L_N is the supernova luminosity at frequency ν and ν_{sn} is the supernova rate (Condon 1992).⁸ Using $\alpha_{nt} = -0.5$, we estimate a current supernova rate in the center of II Zw 40 of $4 \times 10^{-4} \text{ yr}^{-1}$, which is accurate within a factor of a few.

Supernova rates from Starburst 99 models are similar to this value for continuous bursts with ages less than 3.5 Myr and for instantaneous bursts with ages either less than 3.5 Myr or greater than 40.0 Myr (Leitherer et al. 1999). These limits reflect the upper and lower stellar mass limits for supernovae in Starburst 99, which are $100M_{\odot}$ and $8M_{\odot}$. At ages less than 3.5 Myr, the $100M_{\odot}$ stars have not evolved enough to go supernova and at ages greater than 40 Myr, all the stars with masses greater than $8M_{\odot}$ have already exploded. For the continuous burst, only the upper mass limit matters because new clusters are continually being produced.

The age of the burst seen in the radio continuum is most likely less than 3.5 Myr. Based on optical and near-infrared photometry and spectra, Vanzani et al. (1996) estimate that the starburst is less than 4 Myr old. II Zw 40 also shows other signs of a recent burst of star formation: optically visible super star clusters (SSCs) and several ultra compact H II regions, which may harbor young, still obscured, SSCs (Beck et al. 2002; Vanzani et al. 2008). However, our radio continuum age estimate relies on the relationship between the observed synchrotron emission and the supernova rate being roughly the same in II Zw 40 as in the Milky Way. The escape of cosmic ray electrons from II Zw 40 or cosmic ray energy losses in its dense starburst environment (Lacki et al. 2010) could reduce the amount of observed synchrotron emission per supernova.

In contrast to previous results by Beck et al. (2002), we do not find any evidence for discrete sources with purely

⁶ We define the spectral index (α) as $S \propto \nu^{\alpha}$.

⁷ <http://casa.nrao.edu>

⁸ Condon (1992) use the opposite spectral index convention as in this paper. We have rewritten this equation to reflect the convention used here.

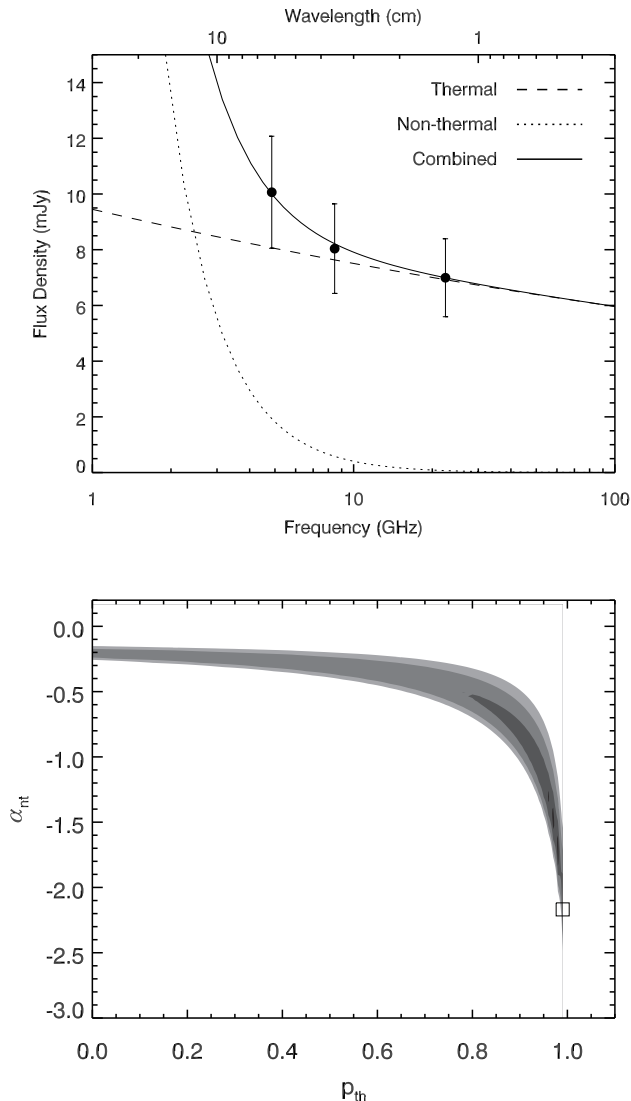


FIG. 4.— *Top*: Radio continuum flux densities in the region corresponding to the 3σ contour in the 1.3 cm matched beam image as a function of frequency. The best combined power law fit is shown as the solid line. The thermal contribution to the fit is shown as a dashed line and the non-thermal contribution to the fit is shown as a dotted line. The error bars on the radio continuum flux densities represent the 20% uncertainty on the photometry rather than the formal error on the flux density. *Bottom*: The χ^2 value as a function of the thermal fraction (p_{th}) and (α_{nt}). The regions from darkest to lightest show 5, 10, 20, and 30 times the minimum χ^2 value. The open square shows the location of the best fit value.

positive spectral indices (and thus optically thick thermal emission) at the size scales probed by our matched beam images. This contrast is consistent with a difference in the adopted 1.3 cm flux scales; Beck et al. adopt a 1.3 cm flux scale a factor of 1.34 greater than the 1.3 cm flux scale adopted here. Using a flux density scale that is too large would increase the derived flux at 1.3 cm and give the appearance of a positive spectral index at 1.3 cm. Our flux density scale calibration is more robust than the flux density scale calibration in Beck et al. because we use a model for the flux calibrator source structure rather than assuming it is a point source. These models were not available when the data used in Beck et al. were

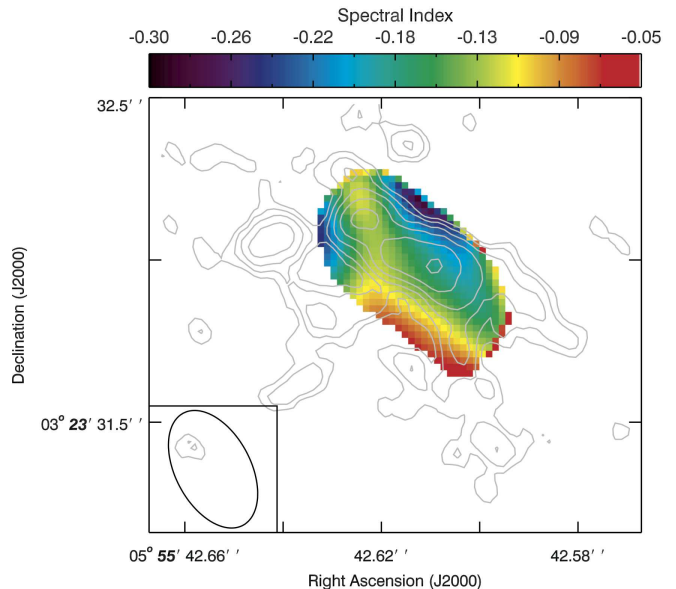


FIG. 5.— Spectral indices between 6.2 cm and 1.3 cm matched $u-v$ coverage images are consistent with optically thin, free-free emission with a small contribution from synchrotron. There are no purely synchrotron sources. Pixels with spectral index errors greater than 0.05 were blanked. The 1.3 cm, robust=0 contours are overlaid.

calibrated. For high angular resolution data, this step is critical because the flux calibrator sources are unlikely to be point sources. We confirmed that the difference between the radio continuum spectrum in Figure 4 and the radio continuum spectrum in Beck et al. (2002) is not due to differences in the $u-v$ range imaged; we created a set of images using our data with the same $u-v$ cutoff as in Beck et al. ($\gtrsim 20k\lambda$) and did not see evidence for any sources with positive spectral indices.

We also created a spectral index map to explore the properties and morphology of the radio continuum emission on smaller scales (Figure 5). Spectral index maps are sensitive to systematic errors. Both of the input images *must* sample the same spatial scales and have the same resolution. Therefore, we cannot use the high resolution, robust=0, 1.3 cm image to create the spectral index maps because the maps at other frequencies would not match its resolution or include the same range of spatial scales. Instead, we created a spectral index map using the matched $u-v$ coverage images (see § 2.1 for details). We blanked any pixels where the formal error on the spectral index was greater than 0.1. While the resolution of these images is two to three times larger than the robust=0, 1.3 cm images, it provides a general picture of the spectral indices for different parts of the central star-forming region of II Zw 40.

As one might expect from the radio continuum spectrum, the spectral index map shows that the central region of II Zw 40 is dominated by optically thin free-free emission with a contribution from synchrotron emission (Figure 5). The indices in this map vary between -0.26 and -0.08. The contribution from synchrotron emission appears to increase towards the northwestern and the northeastern edges of the galaxy, but there do not appear to be any discrete synchrotron dominated ($\alpha \lesssim -0.7$) sources similar to the candidate AGN in the dwarf starburst galaxy He 2-10 (Reines et al. 2011; Reines & Deller

2012) or supernova remnants.

3.1.2. Identifying Radio Continuum Sources

In addition to constraining the dominant continuum emission mechanisms in II Zw 40 (§3.1.1), these radio continuum data are well-suited to measuring the properties of the young massive clusters in this galaxy. The goal of this subsection is to use the robust=0, 1.3 cm radio continuum image with a linear resolution of ~ 7 pc to identify discrete radio continuum sources (which may consist of one or more clusters) and measure their flux densities.

The discrete sources in the robust=0, 1.3 cm image were identified by examining contour plots overlaid on greyscale images of the emission. A source was identified where the presence of a 6σ or greater contour defined a bound region. The sources are shown in Figure 3. We do not have data with sufficient resolution at 3.5 and 6.2 cm to determine the radio continuum spectral index for each source and conclusively identify the emission mechanism. However, we expect that most of the discrete sources identified at 1.3 cm are thermal because the radio continuum spectrum is dominated by free-free emission at that wavelength (§ 3.1.1).

To quantify this, we compare the noise in our robust=0, 1.3 cm with a fiducial H II region (W49) and a fiducial supernova remnant (Cas A). We estimate a 22.46 GHz flux density for a W49A-like region of 0.1 mJy by extrapolating from the measurements of Mezger et al. (1967) assuming strictly thermal emission and accounting for the distance to II Zw 40; this flux is well above our detection limit. Cas A – the brightest Milky Way supernova remnant – would have a flux density of $19 \mu\text{Jy}$ at the distance of II Zw 40, based on the flux density models of Baars et al. (1977). This flux density is below our noise limit in the 1.3 cm, robust=0 image ($24.01 \mu\text{Jy beam}^{-1}$). However, the upper end of the supernova remnant luminosity function may be better sampled in galaxies with high star formation rates (Chomiuk & Wilcots 2009b). For example, the dwarf starburst galaxy NGC 4449 has a supernova remnant with a luminosity five times that of Cas A (Chomiuk & Wilcots 2009a). A supernova remnant with this luminosity would be detected at only the 4σ level in our data. Given that only one of the 43 supernova remnants in the Chomiuk & Wilcots (2009a) sample was brighter than Cas A, it is unlikely that any of our sources are supernova remnants, even if they are as bright as the brightest supernova remnant in NGC 4449.

The complex morphology of the thermal emission in II Zw 40 makes interpretation of the sources difficult. To better characterize the radio continuum sources, we have chosen to divide our source list into two categories: compact or diffuse. We define compact sources as sources whose contours follow the same approximate shape down to the sensitivity limit of the data, while the diffuse sources are the sources whose contours significantly change shape between the highest and lowest contour. While the compact sources (D, E, G, H, I, K) are most likely clusters, the nature of the diffuse sources (A, B, C, F, J) is more uncertain. These sources could be produced by a number of emission mechanisms including a star cluster that is superimposed on diffuse thermal emission, the limb of an ionized gas bubble, diffuse synchrotron emission from a supernova, or the ionized outer

edge of a molecular cloud.

Beck et al. (2002) identify four compact sources in II Zw 40. Their source at $5^{\text{h}}55^{\text{m}}42^{\text{s}}.615$, $03^{\circ}23'32''.02$ (J2000) is source G in this paper. The other three sources identified in that study, which were marginal 3.5σ detections, do not correspond to any of the sources identified in this paper. We suggest that the three low signal to noise detections identified by Beck et al. (2002) are spurious given the robust=0, 1.3 cm image used in our analysis has comparable resolution to the uniformly weighted Beck et al. image and $1/7$ the noise.

We measured 1.3 cm radio continuum flux densities (Table 5) for each source using the program SURPHOT (Reines et al. 2008a), which determines the source flux densities in irregularly shaped regions by summing the flux densities in a user-defined region and subtracting an appropriate background. We used the lowest contour for each source to define the regions. The background for each source was determined using an annulus with the same shape as the source region but a larger size. The size and width of the annulus was chosen for each source to avoid the main body of radio continuum emission in the region and thus accurately reflect the background.

We can compare the global radio continuum emission in the center of II Zw 40 with the emission from the discrete, cluster-sized sources to determine what fraction of the radio continuum emission originates from young massive clusters and what fraction is more diffuse. We find only 44% of the total flux in the central region originates from individual, cluster-sized sources; a large fraction of the radio continuum emission in the center of II Zw 40 is diffuse (Table 5). The diffuse emission in the center of II Zw 40 could be due to a porous ISM allowing ionizing photons to escape the regions in which they were produced. Similar fractions of diffuse emission are seen in the low-metallicity, dwarf, starburst galaxy SBS0335-052 (Johnson et al. 2009). Haro 3 also exhibits evidence for a porous and clumpy interstellar medium (Johnson et al. 2004).

3.1.3. Physical Properties of the Radio Continuum Sources

Given the likelihood that the discrete sources identified here are predominantly thermal at 1.3 cm, we derive the properties of the embedded ionizing clusters using the 1.3 cm continuum flux densities. These properties include an estimate of the number of ionizing photons produced by the young massive stars, the number of equivalent O-stars, the cluster masses for the individual sources, and the star formation rates for the combined sources (Table 6).

The ionizing photon flux can be estimated using

$$N_{ion} \geq 7.56 \times 10^{49} \left(\frac{d}{\text{Mpc}} \right)^2 \left(\frac{1}{1 + (n(\text{He}^+)/n(\text{H}^+))} \right) \times \left(\frac{\nu}{\text{GHz}} \right)^{0.1} \left(\frac{T}{10^4 \text{ K}} \right)^{0.31} \left(\frac{f_\nu}{\text{mJy}} \right) \quad (3)$$

where N_{ion} is the number of ionizing photons, $n(\text{He}^+)/n(\text{H}^+)$ is the ratio of ionized helium to ionized hydrogen, ν is the frequency of the emission, T is the temperature of the region, and f_ν is the flux density of the thermal radio continuum emission (Hunt et al.

2004). This expression is valid for temperatures between 10,000 K and 20,000 K. We assume a temperature for II Zw 40 of 13,000 K, which is the average temperature measured by Walsh & Roy (1993). We use a value of 0.062 for the $n(\text{He}^+)/n(\text{H}^+)$ ratio; this is the average of the $n(\text{He}^+)/n(\text{H}^+)$ ratios found by Walsh & Roy (1993). The resulting number of ionizing photons inferred for each region is given in Table 6. The number of equivalent O-stars in Table 6 was calculated from this number by assuming that one O7.5V star produces 10^{49} ionizing photons per second (Leitherer 1990; Vacca 1994; Vacca et al. 1996). The cluster masses for each source were estimated using the number of ionizing photons for Starburst 99 models of a instantaneous burst of star formation with a metallicity of $Z=0.004$ and an age less than 3.5 Myr.

The number of ionizing photons calculated using Equation 3 is a lower limit. Radio continuum emission is not affected by extinction along the line of sight from the emitting medium. However, there are several other effects that could reduce the number of ionizing photons estimated from the radio continuum. First, ionizing photons could heat the dust rather than ionizing hydrogen, although we expect this effect to be less important for lower metallicity galaxies because of their lower dust-to-gas ratios. For the LMC, 30% of the photons heat the dust rather than ionizing hydrogen (Inoue 2001). This fraction represents an upper limit on the fraction of photons that go into heating dust since the LMC has a metallicity of 1/3 solar ($12 + \log(\text{O}/\text{H}) = 8.3$; Dufour 1984), which is slightly higher than the metallicity of II Zw 40 (1/5 solar). In addition, ionizing photons can leak out of the region if the interstellar medium is clumpy and porous. Approximately 25% of the photons in a region are lost to this effect (Hunter & Gallagher 1997; Relaño et al. 2012). Finally, if the H II region is optically thick (Kobulnicky & Johnson 1999; Johnson & Kobulnicky 2003), then the number of ionizing photons inferred only represents the free-free emission from the surface of the region, rather than the entire three dimensional volume. There is no evidence for this effect on the size scales probed by these observations of II Zw 40, which would manifest as regions with positive spectral indices, indicating self-absorption. Given the possibilities of absorption and leakage of ionizing photons, the overall intrinsic ionizing photon fluxes estimated here could be underestimated by as much as a factor of 2. This value is consistent with the observed ratio of the diffuse to discrete emission determined in § 3.1.2.

The cluster properties estimated above reveal that six out of the eleven sources identified here require fewer than 100 O-stars to produce the measured ionizing photon fluxes. These ionizing photon fluxes correspond to cluster masses of less than $\sim 2.5 \times 10^4 M_{\odot}$ (Leitherer et al. 1999). The relatively low number of O-stars in the sources suggests that the star formation in the center of II Zw 40 is not concentrated in a single massive cluster, but is distributed across the region in several less massive clusters. In addition, there are many extended, faint features, which suggest a porous and clumpy ISM rather than a density- or radiation-bounded region.

Compared to the closest example of a starburst re-

gion, 30 Doradus in the Large Magellanic Cloud, the center of II Zw 40 is the same size as 30 Doradus' central cluster NGC 2070 (~ 40 pc across (Walborn 1991)), but has an ionizing photon flux six times higher (Mills et al. 1978). The individual radio continuum sources in II Zw 40 are similar in size to the core of R136 (2.5 pc; Malumuth & Heap 1994), but three of these sources have ionizing photon fluxes greater than or equal to that of R136 (D, G, and H). All three of these sources are also classified as compact sources, which strengthens our identification of the compact sources as probable young massive clusters. Overall, the center of II Zw 40 appears to be a more extreme starburst than 30 Doradus.

The star formation rates for the combined sources in II Zw 40 were estimated from the ionizing photon flux using

$$\left(\frac{SFR}{M_{\odot} \text{ yr}^{-1}} \right) \sim 7.269 \times 10^{-54} N_{ion} \quad (4)$$

(Murphy et al. 2011).⁹ The star formation rate for the entire central region of II Zw 40 is $0.34 M_{\odot} \text{ yr}^{-1}$; see Table 6 for the star formation rates in the other regions.

Equation (4) assumes a 100 Myr constant star formation rate and solar metallicity. However, simulations by Calzetti et al. (2007) show that star formation rates determined using ionizing photon fluxes only vary by 20% for younger burst ages and metallicities between 1 and 1/5 solar. An estimate of the effect of a shorter burst age can be made by dividing the total cluster mass ($7.4 \times 10^5 M_{\odot}$) by the upper limit on the age of the burst (3.5 Myr; § 3.1.1; Vanzani et al. 1996). This calculation gives a minimum star formation rate of $0.2 M_{\odot} \text{ yr}^{-1}$, which is consistent with the star formation rate estimates derived above. Finally, we note that while the star formation rates calculated above are internally self-consistent, different star formation rate calibrations give star formation rates that vary by a factor of 2 (Leroy et al. 2012).

The star formation rates show that star formation in II Zw 40 is centrally concentrated with a high surface density. The star formation rate for the 20 pc by 42 pc central region of II Zw 40 is a quarter of the total star formation rate of II Zw 40 itself ($\sim 1.4 M_{\odot} \text{ yr}^{-1}$; estimated using a 1.2 cm single dish flux density from Klein et al. 1984 and Equations (3) and (4)) and an eighth of the total star formation rate of the Milky Way ($\sim 2 M_{\odot} \text{ yr}^{-1}$; Chomiuk & Povich 2011). The star formation rate surface density of the central region of II Zw 40 is $520 M_{\odot} \text{ yr}^{-1} \text{ kpc}^{-2}$. This value is twenty times higher than the star formation rate surface density of the extremely low-metallicity (1/50 solar) dwarf starburst galaxy SBS0335-052 (Johnson et al. 2009) and corresponds to the star formation rate surface density values seen in the most strongly starbursting galaxies in Bigiel et al. (2008). The star formation rate surface density of II Zw 40 is greater than the empirical upper limit for star formation rate surface den-

⁹ Star formation rates derived from free-free emission are not affected by dust absorbing the photons emitted by the ionized gas as an H α -based star formation rate would be, and thus do not need a 24 μm -correction term (Murphy et al. 2011). However, the star formation rate may still be an underestimate because it does not account for dust absorption of the ionizing photons from the young massive stars (Leroy et al. 2012).

ties ($45 \text{ M}_\odot \text{ yr}^{-1} \text{ kpc}^{-2}$) derived by Meurer et al. (1997). However, it is less than the upper Eddington limit on the star formation rate surface density set by the effect of radiation pressure on dust ($1000 \text{ M}_\odot \text{ yr}^{-1} \text{ kpc}^{-2}$; Thompson et al. 2005). Therefore, we do not expect a radiation-driven outflow of material from II Zw 40.

3.2. Optical Cluster Properties

A complete picture of the recent star formation in the center of II Zw 40 includes both the properties of the obscured clusters derived from radio continuum in § 3.1 and the properties of the two unobscured optical clusters seen in the *HST* images (Figures 1 and 3). We refer to the two dominant optical clusters as SSC-North and SSC-South. SSC-North is surrounded by bright ionized gas detected at both optical and radio wavelengths, while SSC-South is not associated with strong nebular emission. This section presents estimates of the number of ionizing photons, masses, and ages of the optical clusters from measurements of their optical flux densities.

Optical flux densities of SSC-North and SSC-South were obtained using SURPHOT (Reines et al. 2008a). We used a circular aperture of radius 7 pixels ($0''.175$) which includes the first Airy ring of the PSF. For SSC-South, the background was estimated in an annulus with inner and outer radii of 12 and 18 pixels ($0''.3$ and $0''.45$). For SSC-North, the background was estimated in a more extended annulus with inner and outer radii of 18 and 28 pixels ($0''.45$ and $0''.70$) to avoid the extended ionized gas emission not directly associated with the cluster. Aperture corrections were not applied since they are negligible for such a large aperture as determined using the Tiny Tim web interface.¹⁰ The derived flux densities for the clusters are given in Table 3. The ionizing photon fluxes and number of equivalent O stars was calculated from the foreground Galactic extinction corrected $\text{H}\alpha$ flux using Equations (3) and (7) and an $E(B-V)=0.57$ (Burstein & Heiles 1982).¹¹

Physical properties of the clusters were estimated by comparing the observed photometry to Starburst99 (Version 5.1, Leitherer et al. 1999) and GALEV (Kotulla et al. 2009) evolutionary synthesis models. Details of the models used here can be found in Reines et al. (2010). Briefly, both sets of models are for an instantaneous burst¹² with a Kroupa IMF and use the Geneva evolutionary tracks with a metallicity of $Z = 0.004$ to match the measured metallicity of II Zw 40 ($12 + \log(\text{O}/\text{H}) = 8.09$; Guseva et al. 2000). Stellar and nebular continuum are included in both sets of models, however, the GALEV models also include emission lines (e.g. Anders & Fritze-v. Alvensleben 2003).

¹⁰ <http://www.stsci.edu/software/tinytim/tinytim.html>

¹¹ We use the Burstein and Heiles $E(B-V)$ values because the $E(B-V)$ values from Schlegel et al. (1998) and its re-calibration by Schlafly & Finkbeiner (2011) are larger than the average total extinction we find in the near-infrared for II Zw 40 by comparing our radio continuum data and near-infrared data from the literature (see § 4.2.2).

¹² For SSC-North, the choice of instantaneous or continuous burst of star formation does not affect the derived age. For SSC-South, a continuous burst of star formation would require an unrealistically old age for the cluster ($\gtrsim 1\text{Gyr}$), given that the current burst of star formation in II Zw 40 is less than 4 Myr old (Vanzi et al. 1996).

Ages of the clusters were estimated using the equivalent width (EW) of $\text{H}\alpha$. The EWs were calculated as $(f_{F658N} - f_{cont})\Delta\lambda_{F658N}/f_{cont}$ where f_{F658N} is the flux density through the F658N filter, $\Delta\lambda_{F658N}$ is the width of the F658N filter (78\AA , *HST* ACS Cycle 18 Instrument Handbook, Table 5.1), and f_{cont} is the continuum (stellar + nebular) flux density. The archival *HST* ACS observations did not include a corresponding continuum filter for the F658N filter. Therefore, the continuum was estimated by interpolating between the flux densities in the adjacent F555W and F814W filters. The $\text{H}\alpha$ EWs of SSC-North and SSC-South are $\sim 460\text{\AA}$ and $\sim 50\text{\AA}$, respectively. The corresponding ages inferred from the Starburst99 models are $\lesssim 5.0$ Myr for SSC-North and $\sim 9.4_{-1.0}^{+1.4}$ Myr for SSC-South.

The presence of emission lines in the F555W and F814W filters may affect the estimated continuum and thus the $\text{H}\alpha$ -derived optical cluster properties. While SSC-South is old enough that line contamination is minimal, SSC-North is young enough that line contamination could significantly affect the continuum estimate (see Figure 11 in Reines et al. 2010). We estimate the line contamination for the SSC-North F555W and F814W measurements using the line contamination calculated in Table 4 of Reines et al. (2010) for a cluster in the galaxy NGC 4449 with a similar age and metallicity. From this table, we find that line emission could contribute about 25% of the flux in the F814W filter and about 63% of the flux in the F555W filter for SSC-North. After correcting the flux for SSC-North in these filters for the estimated line contamination, the resulting $\text{H}\alpha$ fluxes (and number of ionizing photons and number of O stars) only differ by 10% from the estimates given in our Table 7. The resulting $\text{H}\alpha$ equivalent width changes from $\sim 460\text{\AA}$ to $\sim 986\text{\AA}$, but age limit derived from this quantity does not change significantly ($\lesssim 4\text{Myr}$ instead of $\lesssim 5\text{Myr}$).

To estimate the extinction of the clusters, we compared the observed $m_{F555W} - m_{F814W}$ color to the Starburst99 and GALEV model colors. Figure 6 shows the model colors as a function of age, accounting for Galactic foreground reddening using the extinction curve of Cardelli et al. (1989). Color evolutionary tracks using $E(B-V) = 0.82$ (Schlegel et al. 1998) and $E(B-V) = 0.57$ (Burstein & Heiles 1982) are shown for both the Starburst99 and GALEV models. Both clusters appear to have minimal internal reddening. However, it is possible that some of the optical light is completely absorbed (and not impacting our measured extinction) in a dense and clumpy ISM (e.g. Reines et al. 2008b), especially for the younger SSC-North.

Masses of the clusters were estimated by comparing the observed flux densities in the F555W and F814W filters to the model flux densities for a 10^5 M_\odot cluster. Lower limits of the cluster masses were obtained by assuming no internal extinction and a Galactic foreground reddening of $E(B-V) = 0.57$. For SSC-North, we used the GALEV model since emission lines are significant at such a young age (e.g., Reines et al. 2010) and obtained a minimum mass of $0.9 \times 10^5 \text{ M}_\odot$. For SSC-South, we obtained a minimum mass of $1.6 \times 10^5 \text{ M}_\odot$. The GALEV and Starburst99 models give nearly the same result for this cluster since the relative importance of nebular emission is significantly diminished by ~ 10 Myr. Table 7

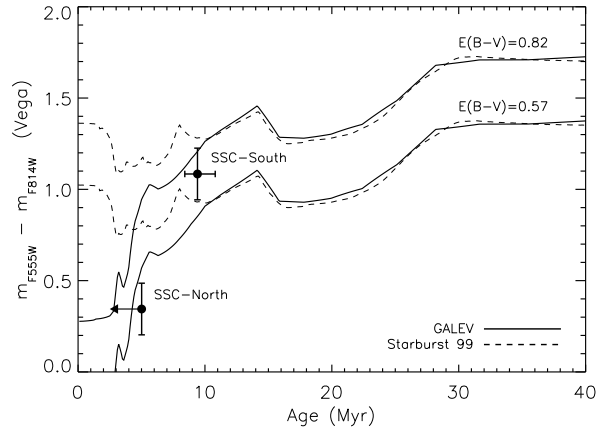


FIG. 6.— The north and south optical clusters in II Zw 40 are young with ages of $\lesssim 5.0$ Myr and $9.4^{+1.4}_{-1.0}$ Myr, respectively. The ages were determined using the $H\alpha$ equivalent width (see § 3.2 for details). The solid lines show the GALEV models that include emission lines in addition to nebular continuum and the dashed lines show the Starburst99 models that only include nebular continuum. The two optical clusters are indicated. We show models using the Burstein & Heiles (1982) extinction, $E(B-V)=0.57$, and the Schlegel et al. (1998) extinction, $E(B-V)=0.82$.

gives an overview of the derived properties of the optical clusters.

The masses and ages of the optical clusters derived here agree with other estimates of their age and mass. Using $\text{Br}\gamma$ observations of SSC-North, Vanzì et al. (2008) derive an upper limit on its age of 3 Myr, which agrees with the age derived above. Using our data and the same size aperture as Vanzì et al. ($15''$ instead of $0.35''$), we derive a mass for SSC-North of $(1 - 5) \times 10^6 M_{\odot}$, which is also in agreement with their mass estimate of $1.7 \times 10^6 M_{\odot}$. For SSC-South, Vanzì et al. find an age of 6 to 7 Myr and a mass of $1.3 \times 10^5 M_{\odot}$, which are similar to our derived values.

A comparison of the optically visible clusters and the radio sources shows that the optical clusters have ionizing photon fluxes (derived from $H\alpha$) similar to the fainter radio continuum sources (Figure 7). The brightest 3 radio continuum sources have 2-4 times more ionizing photons than the brightest optical cluster. However, the number of ionizing photons may be underestimated by a factor of a few for the optical clusters. First, we have chosen an aperture including only the cluster and have excluded much of the surrounding emission; this effect may be particularly important for SSC-N. Second, the foreground extinction may be underestimated; we use the Burstein & Heiles (1982) value rather than the larger Schlegel et al. (1998) or Schlafly & Finkbeiner (2011). However, we believe our foreground extinction estimate is appropriate because larger values lead to more extinction in the infrared than we measure for II Zw 40 (§ 4.2.2).

The brightest clusters seen in the radio may be producing more ionizing photons than the brightest optical cluster because of differences in either the ages of the clusters or the mass distribution of the clusters. As clusters age, the number of ionizing photons decreases because the most massive stars in the cluster die first. Leitherer et al. (1999) shows that for a cluster of a given mass the number of ionizing photons as a function of time is roughly

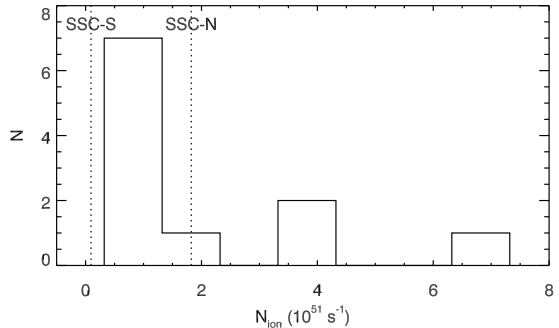


FIG. 7.— In the center of II Zw 40, the optical clusters have ionizing photon fluxes similar to the fainter radio continuum sources. The histogram shows the radio continuum ionizing photon fluxes determined in § 3.1.2. The ionizing photon fluxes for the optical clusters from § 3.2 are marked with dotted lines and labeled with the cluster name. The ionizing photon flux from SSC-N is a lower limit.

constant for the first 4 Myr of a burst. Depending on the relative ages of the clusters seen in the radio continuum the difference in the number of ionizing photons between the radio and optical clusters is between 1.5 times (for a radio continuum cluster age of 3 Myr and an optical cluster age of 5 Myr) and 5.6 times (for a radio continuum cluster age of 1 Myr and an optical cluster age of 5 Myr). The mass distribution of the clusters may also change with time, which would lead to differences in the ionizing photon flux between the younger, still obscured radio cluster population and the slightly older, less obscured optical cluster population. If the star formation in the center of II Zw 40 is ramping up and producing more massive clusters, the radio should see an increase in the number of ionizing photons because it is probing a younger generation that is producing more ionizing photons because there are more massive clusters than in the optical. On other hand, if the star formation rate is roughly constant, the difference between the radio and optical sources could reflect the destruction of clusters (Fall et al. 2009). Unfortunately, we do not have enough information here to disentangle these possibilities.

4. DISCUSSION

This section uses the properties of the radio continuum emission (§ 3.1), and the optical clusters (§ 3.2) to explore star formation in the center of II Zw 40. Our goal is to identify whether star formation in this low-metallicity dwarf starburst galaxy is different than star formation in other environments, and if so, what the differences are. First, we quantify the properties of the young massive cluster population in II Zw 40 using the H II region luminosity function (§ 4.1). Then, we discuss the internal extinction due to dust in II Zw 40 (§ 4.2).

4.1. The H II Region Luminosity Function

In this section, we derive the H II region luminosity function for the central region of II Zw 40 using its radio continuum source properties (§ 3.1.2). The resolution of our data is well-matched with the size scales of clusters allowing us to directly probe the cluster luminosity function. We compare the derived H II region luminosity function for II Zw 40 with H II region luminosity functions in other galaxies to determine whether the physical

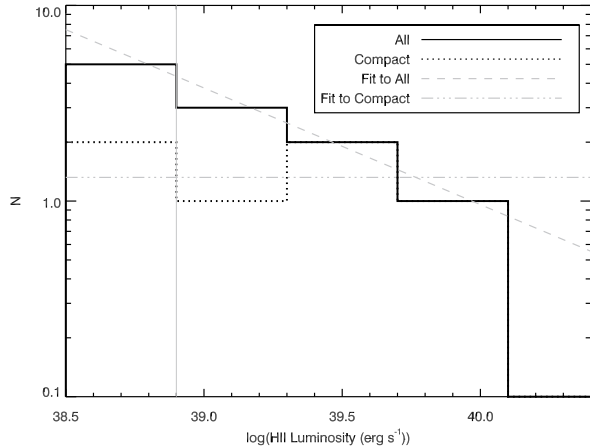


FIG. 8.— The slope of the H II region luminosity function for the radio continuum sources identified in II Zw 40 is flatter than those found for earlier type galaxies. The H II region luminosity function for all sources in II Zw 40 is shown as a solid line, while the H II region luminosity function for just the compact sources is a dotted line. The fits to the luminosity functions have slopes of -1.59 ± 0.09 for all sources (dash-dotted line) and -1.00 ± 0.43 if only compact sources are included (dash-triple dotted line). Both fits exclude the faintest luminosity bin, which is below the 3σ completeness limit (shown here as a thin, grey, vertical line). Earlier type galaxies tend to have steeper slopes (~ -2) (Kennicutt et al. 1989). This effect has been attributed to cluster sampling statistics (Oey & Clarke 1998). Later type galaxies tend to have brighter clusters, which tends to produce a flatter luminosity function. Note that fits to luminosity functions in $\log(N) - \log(L)$ result in an apparent slope of $\alpha + 1$ because the luminosity function is defined in linear intervals, but the plot is in logarithmic intervals.

conditions in II Zw 40 may impact the cluster population.

A fundamental issue with luminosity functions in dwarf galaxies is that there will be few sources due to the low mass of these galaxies. However, it is still important to build up statistics on their luminosity functions because these galaxies have physical environments that differ from more massive systems.

H II region luminosity functions are typically modeled as power laws:

$$N(L) = AL^\alpha dL \quad (5)$$

where $N(L)$ is the number of clusters in the interval L to $L + dL$, α is the slope,¹³ and A is the normalization constant (Kennicutt et al. 1989). The fitted H II region luminosity function slopes are -1.59 ± 0.09 for all the sources and -1.00 ± 0.43 for only the compact sources (Figure 8). These fits exclude sources below the completeness limit.

Determining the slope is possible because it relies on the distribution of all the sources rather than the number of counts in a particular luminosity bin. To demonstrate this, we carried out Monte Carlo simulations which generated 1000 H II region luminosity functions drawn from a power law distribution with the same number of sources as above and fit the slope of each luminosity function. We used two power law distributions: one with a slope

¹³ Unfortunately, the variable α is commonly used for both the slope of the H II region luminosity function and the slope of the radio continuum spectrum. We retain the common usage of these variables to avoid confusion with other papers in the literature and rely on context to distinguish them.

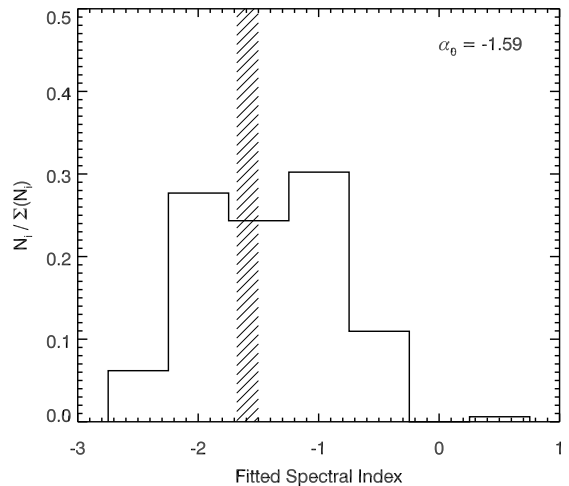
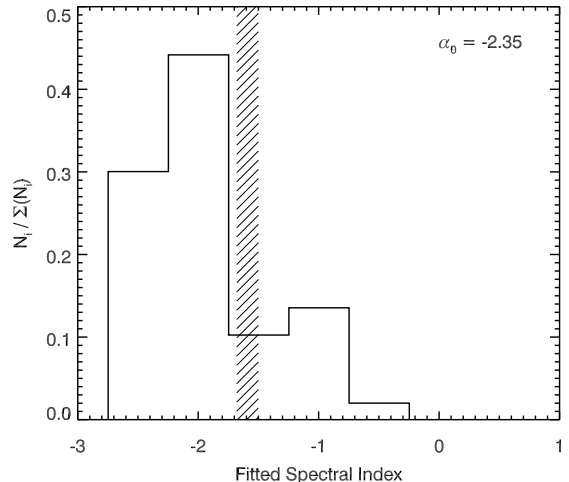


FIG. 9.— Even with the small sample here we can determine the slope of the H II region luminosity function. This plot shows the distribution of the slopes fit to simulated H II region luminosity functions with the same number of sources as we observe. The H II region luminosity functions were drawn from two power law distributions: one with a slope of -2.35 and the other with a slope of -1.59 . The fitted slope values from the Monte Carlo simulation tends to cluster around the true slope value. The slope value determined from our data is shown as the hashed region. We would measure this value only 7% of the time if the true slope was -2.35 .

of -2.35 , which is comparable to the “typical” slope for a cluster mass function (Kennicutt & Evans 2012), and the other with a slope of -1.59 , the slope derived above for the entire sample. Even with a small number of sources, the distribution of fitted slopes for the simulated H II region luminosity functions tends to cluster around the true slope of the H II region luminosity function (Figure 9). If the true slope were -2.35 , the data would only yield a fit with a slope of -1.59 ± 0.09 7% of the time.

The slope of the H II region luminosity function tends to decrease with the Hubble type of the galaxy; Sa/Sb galaxies have much steeper slopes than irregular galaxies (Kennicutt et al. 1989). The slopes of the H II region luminosity functions for two large spiral galaxies, M101 and M31, are -2.3 ± 0.2 and -2.1 ± 0.2 , respectively (Kennicutt et al. 1989), while the slope for the LMC is

-1.75 ± 0.15 (Kennicutt et al. 1989). For a sample of irregular galaxies, the average slope is -1.0 ± 0.1 for a sample with no turnover in the luminosity function and -1.5 ± 0.1 for a sample with a turnover in the luminosity function (Youngblood & Hunter 1999).

We cannot directly compare the slope of our H II luminosity function to the slopes determined by Kennicutt et al. (1989) and Youngblood & Hunter (1999) because we have much higher resolution (~ 7 pc) than these papers (~ 30 pc). H II regions identified at low resolutions (30-70 pc) separate into individual H II regions at higher resolutions (5-10 pc) causing the slope of the luminosity function to steepen (Pleuss et al. 2000; Scoville et al. 2001). However, the relative trend of flatter slopes for later type galaxies should be the same for a data set with uniform resolution. Studies of H II region luminosity functions with 10 pc resolution are rare. In one example, Gutiérrez et al. (2011) derive H II region luminosity functions using high resolution *HST* data. They find a similar trend to Kennicutt et al. (1989): the irregular galaxy NGC 4449 has a flatter luminosity function slope ($\alpha = -1.43$) than the spiral galaxy M51 ($\alpha = -1.79$).

The flat slope of the H II region luminosity function in II Zw 40 may be due to relatively more clusters with high ionizing photon fluxes. This could result from either more massive stars per cluster (i.e., a top-heavy IMF) or a higher relative number of massive clusters than in normal spiral galaxies (Kennicutt et al. 1989). The latter possibility is more likely because the IMF in most galaxies appears to be roughly constant (Bastian et al. 2010). Stochastic models of H II region luminosity functions suggest more massive clusters in a galaxy produce flatter luminosity function slopes (Oey & Clarke 1998). However, the relationship between H II region luminosity functions and cluster mass functions depends on the sampling of the IMF to convert ionizing photon fluxes to masses. This complexity makes any conclusions on the form of the cluster mass function uncertain.

As discussed in the introduction, there are several mechanisms that could lead to galaxies like II Zw 40 having a disproportionate number of more massive clusters, including: low large-scale shear in a quiescent galaxy (Weidner et al. 2010), high molecular gas surface densities leading to less effective radiation pressure (Krumholz et al. 2010), or high ISM pressures (Elmegreen & Efremov 1997). II Zw 40 is in the end stages of a merger as evidenced by its optical (Figure 1) and neutral hydrogen emission (van Zee et al. 1998). Therefore, we conclude that the most likely explanation for the possible presence of more massive clusters in II Zw 40 is high ISM pressures due to the interaction rather than low large-scale shear, which is unlikely given the merger history of II Zw 40, or less effective radiation pressure, which requires a high dust opacity.

4.2. Internal Extinction

This section uses the free-free emission in the radio with the H α emission in the optical (as well as other hydrogen recombination lines in the optical and infrared) to measure the internal extinction in II Zw 40. Free-free emission is produced by the same electrons that produce H α emission in the optical; both of these emission mechanisms fundamentally trace the same physical re-

gion. However, free-free emission is not attenuated by dust, unlike H α emission (or any of the standard Balmer, Paschen, or even Brackett transitions). Therefore, the internal dust extinction can be estimated by comparing the H α emission predicted by the free-free emission in the radio to the observed H α emission in the optical. Section 4.2.1 estimates the extinctions for the individual sources in II Zw 40, while §4.2.2 determines the internal extinction as a function of wavelength integrated over the central region of II Zw 40.

There are two key facts to remember about internal extinctions derived using this method. First, the internal extinction is a convolution of the properties of the dust *and* the geometry of the dust and the young massive stars, not just the properties of the dust alone. In other words, extinction estimates of this type are luminosity weighted: regions with a greater contribution to the total light will dominate. A second related point is that this extinction estimate will be a lower limit for the total extinction in the galaxy if photons are absorbed by dust or escape the region rather than ionizing hydrogen.

4.2.1. Individual source extinction values

The internal extinctions for the individual radio continuum sources defined in § 3.1.2 were calculated in the following way:

1. We measured the optical flux densities for each radio continuum source using the *HST* ACS data (Table 8). The continuum for the F658N filter was estimated using the same method as in §3.2.
2. We corrected the optical H α fluxes for foreground Galactic extinction using

$$f_{H\alpha,c} = f_{H\alpha} 100^{A_{gal,H\alpha}/5} \quad (6)$$

where $f_{H\alpha,c}$ is the H α flux corrected for foreground Galactic extinction, $f_{H\alpha}$ is the measured H α flux, and $A_{gal,H\alpha}$ is the foreground Galactic extinction. (Table 9). The foreground extinction at the position of II Zw 40 is $E(B-V) = 0.57$ (Burstein & Heiles 1982), which translates to an extinction at the wavelength of H α of 1.4 magnitudes, assuming an $R_V=3.1$ Milky Way extinction curve (Cardelli et al. 1989).

3. We calculated the expected H α flux based on the radio continuum for each source using the high resolution 1.3 cm data and the following equation:

$$\left(\frac{f_{H\alpha,est}}{10^{-12} \text{ erg cm}^{-2} \text{ s}^{-1}} \right) = 0.864 \left(\frac{1}{1 + (n(H e^+)/n(H^+))} \right) \left(\frac{T}{10^4 \text{ K}} \right)^{-0.617} \left(\frac{\nu}{\text{GHz}} \right)^{0.1} \left(\frac{f_\nu}{\text{mJy}} \right) \quad (7)$$

where $f_{H\alpha,est}$ is the predicted H α flux and f_ν is the flux density of the thermal radio continuum emission (Hunt et al. 2004). This expression is accurate for temperatures between 10,000 K and 20,000 K and densities between 100 and 1000 cm^{-3} . We use the same helium fraction, temperature, and frequency as in Section 3.1.2 for this calculation.

4. We calculated the internal extinction using the Galactic foreground corrected optical H α flux and the expected H α flux based on the radio continuum using:

$$A_{H\alpha} = 2.5 \log \left(\frac{f_{H\alpha,est}}{f_{H\alpha,c}} \right) \quad (8)$$

where $A_{H\alpha}$ is the extinction in magnitudes.

While many dwarf galaxies can be assumed to be transparent (Wang & Heckman 1996; Bell 2003), the internal extinctions calculated for II Zw 40 show that this galaxy is more opaque than the typical dwarf galaxy (Table 9). The H α extinction derived for the entire central region implies that only 30% of the ionized gas is visible in the optical. This high level of internal extinction underscores how crucial long wavelength observations are for studying these regions.

Other estimates of the internal extinction in II Zw 40 from optical hydrogen recombination lines agree with our results. They range between $A_V = 0.23 - 1.23$ mag with a mean of approximately 0.83 mag (Sargent & Searle 1970; Wynn-Williams & Becklin 1986; Joy & Lester 1988; Walsh & Roy 1993; Vanzì et al. 1996; Davies et al. 1998). In contrast, much higher values of the internal extinction are derived from dust emission models: $A_V \sim 30$ (Hunt et al. 2005). The difference between the optical and dust-derived extinctions suggests that dense gas clumps in II Zw 40 absorb a significant number of photons that would otherwise ionize hydrogen. The extinction inferred from the infrared reflects the photons that are absorbed by dust, but the extinction inferred from the optical recombination lines can only be produced by photons escaping between the dust clumps to ionize hydrogen, lowering the total extinction seen along the line of sight. This trend for extinctions is commonly seen in starburst galaxies (Gordon et al. 1997; Calzetti 2001; Reines et al. 2008b) and in other dwarf starburst galaxies like Haro 3 and SBS0335-052 (Johnson et al. 2004; Reines et al. 2008b; Johnson et al. 2009) and is likely produced by a porous and clumpy interstellar medium.

4.2.2. Internal Extinction Curve Integrated Over the Central Region

The total internal extinction – the internal extinction integrated over the center of II Zw 40 as a function of wavelength – can be measured by comparing our radio continuum measurements to hydrogen recombination line measurements in the optical and near-infrared from the literature and subtracting an estimate of the foreground Milky Way extinction. We use the hydrogen recombination line measurements from Izotov & Thuan (2011) because these data offer uniform coverage over a wide wavelength range (0.36 to 2.46 μm).

We used apertures matching those used by Izotov & Thuan (2011) to measure corresponding radio continuum flux densities. The optical spectra had an extraction aperture of 1".1 by 6" at a position angle of 214° and the near-infrared spectra had an extraction aperture of 1".5 by 4" at a position angle of 128° (Y. Izotov, 2011, private communication). The H α fluxes estimated from our radio continuum data for the optical and near-infrared apertures are

4.76×10^{-12} and 4.15×10^{-12} erg cm $^{-2}$ s $^{-1}$, respectively. We used the Case B, 100 cm $^{-3}$, 10,000 K line ratios from Storey & Hummer (1995) and Equation (7) to determine the estimated fluxes for the other hydrogen recombination lines from our radio continuum data.

The near-infrared and optical spectra in Izotov & Thuan (2011) were taken by two different instruments with two different apertures and need to be put on the same flux density scale. Comparing the spectra requires taking into account the distribution of the ionized gas emission. If we assume that the radio continuum and Paschen ϵ line have the same distribution, the flux for the Paschen ϵ in the near-infrared aperture should be 0.935 times the flux of that line in the optical aperture.¹⁴ The scaling used in Izotov & Thuan (2011), which was based on the flux of the [SIII] 0.953 μm line in the two spectra and did not account for the spatial distribution of emission, produces a Paschen ϵ line flux in the near-infrared aperture that is 0.842 times that of the Paschen ϵ line flux in the optical aperture. Multiplying the near-infrared values given in Table 3 of Izotov & Thuan (2011) by a factor of 1.11 reproduces the expected line flux ratio between the Paschen ϵ line fluxes in the near-infrared and optical apertures (0.935).

We calculated the internal extinction for II Zw 40 as in Section § 4.2.1 using our radio continuum data, the re-scaled optical and near-infrared line fluxes from Izotov & Thuan (2011), and an estimate of the foreground Milky Way extinction (Figure 10). The integrated internal extinction curve for II Zw 40 is consistent with the metallicity-independent internal extinction curve typical of starburst galaxies (Gordon et al. 1997). Therefore, the internal extinction curve in II Zw 40 appears to be governed by the starburst and metallicity plays a secondary role. The internal extinction curves for starburst galaxies are thought to be the result of the starburst clearing the dust out of the central burst region leaving behind a shell of clumpy dust (see § 4.2 and Figure 8 in Calzetti et al. 2000), which is consistent with our model for the internal extinction in II Zw 40 in § 4.2.1.

Izotov & Thuan (2011) find that II Zw 40 has similar internal extinction in the near-infrared and the optical. Our internal extinction curve demonstrates that, when the correct scaling factors are applied to their data, the extinction in the near-infrared is significantly less than the extinction in the optical.

5. SUMMARY AND CONCLUSIONS

This paper presented high resolution radio continuum observations from the VLA and optical observations from *HST* of the young massive cluster population of the prototypical dwarf starburst galaxy II Zw 40. These observations were used to quantify the properties of star formation in this extreme galactic environment and compare them to the star formation properties of other galaxies.

We found that the radio continuum spectrum of the central portion of II Zw 40 is dominated by free-free

¹⁴ The internal extinction should not significantly change the distribution of Paschen ϵ emission compared to the radio continuum because we are considering a longer wavelength line that is much less affected by extinction.

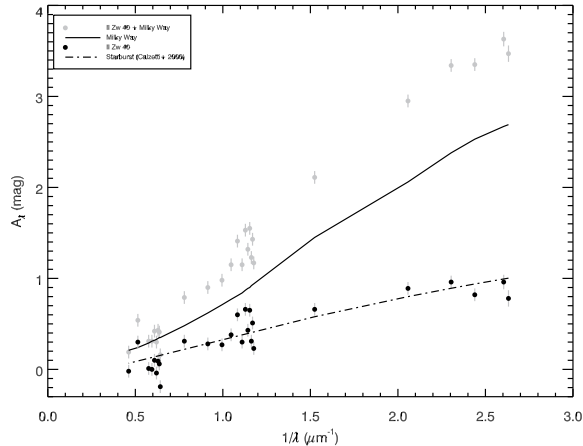


FIG. 10.— The variation of internal extinction with inverse wavelength for II Zw 40 is consistent with that of a typical starburst galaxy. The gray points show the total extinction (Milky Way foreground plus II Zw 40 internal extinction) determined by comparing the radio continuum emission presented in this paper with optical and near-infrared line fluxes from Izotov & Thuan (2011). The radio fluxes were measured using the same apertures as in the optical and near-infrared spectra. The near-infrared line fluxes have been scaled so that the near-infrared Paschen ϵ flux matches the expected near-infrared Paschen ϵ flux based on the distribution of the ionized gas emission and the sizes and orientations of the near-infrared and optical apertures. The solid black line shows the Cardelli et al. (1989) Galactic extinction curve ($R_v = 3.1$, $E(B-V) = 0.57$). The estimated internal extinction due solely to II Zw 40 (total extinction minus the foreground Milky Way extinction) is shown as black points. A fitted starburst extinction curve is shown as a dash-dot line (Calzetti et al. 2000).

emission from gas ionized by young massive stars. The relatively weak synchrotron emission implies that the supernova rate is low and thus that the current burst of star formation is still relatively young ($\lesssim 3.5$ Myr). The morphology of the radio continuum distribution shows that the star formation in the central part of II Zw 40 is clumpy and distributed. The total ionizing photon flux for the entire central region of II Zw 40 is comparable to that of NGC 2070, the central cluster powering the 30 Doradus region in the LMC, and the star formation rate surface density is extremely high ($520 M_\odot \text{ yr}^{-1} \text{ kpc}^{-2}$). There are 3 sources with ionizing photon fluxes comparable to the very center of NGC 2070 (R136) in 30 Doradus, but a majority of the sources have fewer ionizing photons. Discrete, cluster-sized sources also only account for roughly half the emission; the remainder is diffuse. The diffuse emission could be due to leakage of ionizing photons from the main star-forming regions.

In the optical, there are two dominant clusters in the central star-forming region of II Zw 40, with the southern cluster having an older estimated age than the northern cluster (9.4 Myr and $\lesssim 5.0$ Myr, respectively). The lower limits on the optical cluster ionizing fluxes (which are correlated with the cluster mass) are comparable to the ionizing fluxes of the fainter radio continuum sources. Given that the youngest clusters (identified in the radio)

are also the most massive implies either an evolution in the star formation rate in the center of II Zw 40 (i.e. star formation is still ramping up) or an evolution of the cluster population (i.e. disruption of the older clusters or lower ionizing photons fluxes from older clusters).

Monte Carlo simulations verify that the H II region luminosity function is flatter than the typical cluster mass function ($\alpha = -1.59 \pm 0.09$ instead $\alpha \sim -2.35$), reflecting the general trend of later type galaxies having flatter H II region luminosity functions. This trend implies that II Zw 40 has relatively more massive clusters than an earlier-type galaxy. These massive clusters may be the result of the high ISM pressures produced by the merger that created II Zw 40. This conclusion relies on being able to convert ionizing photon fluxes to masses, which assumes that the IMF is normal and well-populated.

The extinctions derived for II Zw 40 show that, even in low-metallicity galaxies, young massive star-forming regions are relatively opaque. Only thirty percent of the ionizing photons in the center of II Zw 40 are visible in the optical. The dust extinction in II Zw 40 is consistent with the clumpy and porous dust seen in other starburst galaxies, regardless of their metallicity. The measured extinction values appear to be luminosity weighted and thus biased towards regions with little dust.

Although disentangling the relative effects of mass and metallicity is difficult, the star formation properties of II Zw 40 described above appear to be the result of the starburst ignited by its recent merger; the low mass and low metallicity of this galaxy only appear to play a secondary role. II Zw 40's dust extinction is more similar to the values seen in higher mass, higher metallicity starburst galaxies than to the values seen in other low-metallicity dwarf galaxies. Its H II region luminosity function is relatively flat, which is similar to that seen in irregular galaxies. However, this is likely the effect of the high ISM pressures created in merger-related starburst rather than galaxy mass or metallicity.

Merger-driven bursts of star formation similar to the burst in II Zw 40 may be more common at high redshifts. Evidence from optical studies suggests that massive galaxies at high redshift have morphologies similar to today's low-mass irregular galaxies rather than to today's spirals (Elmegreen et al. 2009). Dwarf galaxies are also the most abundant type of galaxy in the universe (Bergvall 2012). While the merger rate is relatively low today, higher merger rates in the past mean that star formation events like the one in II Zw 40 may have been more likely in the early universe (Lotz et al. 2011).

A.A.K. thanks Laura Chomiuk, Deidre Hunter, Remy Indebetouw, Suzanne Madden, Elizabeth Stanway, and David Whelan for helpful discussions and Adam Leroy for detailed comments on an earlier draft. K.E.J. acknowledges support provided by NSF through CAREER award 0548103 and the David and Lucile Packard Foundation through a Packard Fellowship. A.E.R. gratefully acknowledges support provided by NASA through the Einstein Fellowship Program grant PF1-120086 and from a NASA Earth and Space Science Fellowship.

REFERENCES

- Anders, P., & Fritze-v. Alvensleben, U. 2003, *A&A*, 401, 1063
 Baars, J. W. M., Genzel, R., Pauliny-Toth, I. I. K., & Witzel, A. 1977, *A&A*, 61, 99

- Bastian, N., Covey, K. R., & Meyer, M. R. 2010, *ARA&A*, 48, 339
- Beck, R., & Krause, M. 2005, *Astronomische Nachrichten*, 326, 414
- Beck, S. C., Turner, J. L., Langland-Shula, L. E., Meier, D. S., Crosthwaite, L. P., & Gorjian, V. 2002, *AJ*, 124, 2516
- Bell, E. F. 2003, *ApJ*, 586, 794
- Bergvall, N. 2012, *Star Forming Dwarf Galaxies*, ed. P. Papaderos, S. Recchi, & G. Hensler, 175
- Bigiel, F., Leroy, A., Walter, F., Brinks, E., de Blok, W. J. G., Madore, B., & Thornley, M. D. 2008, *AJ*, 136, 2846
- Bolatto, A. D., Leroy, A. K., Rosolowsky, E., Walter, F., & Blitz, L. 2008, *ApJ*, 686, 948
- Brinks, E., & Klein, U. 1988, *MNRAS*, 231, 63P
- Burstein, D., & Heiles, C. 1982, *AJ*, 87, 1165
- Calzetti, D. 2001, *PASP*, 113, 1449
- Calzetti, D., Armus, L., Bohlin, R. C., Kinney, A. L., Koornneef, J., & Storchi-Bergmann, T. 2000, *ApJ*, 533, 682
- Calzetti, D., Kennicutt, R. C., Engelbracht, C. W., Leitherer, C., Draine, B. T., Kewley, L., Moustakas, J., Sosey, M., Dale, D. A., Gordon, K. D., Helou, G. X., Hollenbach, D. J., Armus, L., Bendo, G., Bot, C., Buckalew, B., Jarrett, T., Li, A., Meyer, M., Murphy, E. J., Prescott, M., Regan, M. W., Rieke, G. H., Roussel, H., Sheth, K., Smith, J. D. T., Thornley, M. D., & Walter, F. 2007, *ApJ*, 666, 870
- Cardelli, J. A., Clayton, G. C., & Mathis, J. S. 1989, *ApJ*, 345, 245
- Chomiuk, L., & Povich, M. S. 2011, *AJ*, 142, 197
- Chomiuk, L., & Wilcots, E. M. 2009a, *AJ*, 137, 3869
- , 2009b, *ApJ*, 703, 370
- Condon, J. J. 1992, *ARA&A*, 30, 575
- Davies, R. I., Sugai, H., & Ward, M. J. 1998, *MNRAS*, 295, 43
- Deeg, H., Brinks, E., Duric, N., Klein, U., & Skillman, E. 1993, *ApJ*, 410, 626
- Dufour, R. J. 1984, in *IAU Symposium*, Vol. 108, *Structure and Evolution of the Magellanic Clouds*, ed. S. van den Bergh & K. S. D. de Boer, 353–360
- Duric, N., Bourneuf, E., & Gregory, P. C. 1988, *AJ*, 96, 81
- Elmegreen, B. G., & Efremov, Y. N. 1997, *ApJ*, 480, 235
- Elmegreen, D. M., Elmegreen, B. G., Marcus, M. T., Shahinyan, K., Yau, A., & Petersen, M. 2009, *ApJ*, 701, 306
- Fall, S. M., Chandar, R., & Whitmore, B. C. 2009, *ApJ*, 704, 453
- Galliano, F., Madden, S. C., Jones, A. P., Wilson, C. D., & Bernard, J. 2005, *A&A*, 434, 867
- Galliano, F., Madden, S. C., Jones, A. P., Wilson, C. D., Bernard, J., & Le Peintre, F. 2003, *A&A*, 407, 159
- Gil de Paz, A., Madore, B. F., & Pevunova, O. 2003, *ApJS*, 147, 29
- Gordon, K. D., Calzetti, D., & Witt, A. N. 1997, *ApJ*, 487, 625
- Greisen, E., ed. 2010, *AIPS COOKBOOK* (NRAO)
- Guseva, N. G., Izotov, Y. I., & Thuan, T. X. 2000, *ApJ*, 531, 776
- Gutiérrez, L., Beckman, J. E., & Buenrostro, V. 2011, *AJ*, 141, 113
- Hunt, L., Bianchi, S., & Maiolino, R. 2005, *A&A*, 434, 849
- Hunt, L. K., Dyer, K. K., Thuan, T. X., & Ulvestad, J. S. 2004, *ApJ*, 606, 853
- Hunter, D. A., & Gallagher, III, J. S. 1997, *ApJ*, 475, 65
- Inoue, A. K. 2001, *AJ*, 122, 1788
- Izotov, Y. I., & Thuan, T. X. 2011, *ApJ*, 734, 82
- Johnson, K. E., Hunt, L. K., & Reines, A. E. 2009, *AJ*, 137, 3788
- Johnson, K. E., Indebetouw, R., Watson, C., & Kobulnicky, H. A. 2004, *AJ*, 128, 610
- Johnson, K. E., & Kobulnicky, H. A. 2003, *ApJ*, 597, 923
- Joy, M., & Lester, D. F. 1988, *ApJ*, 331, 145
- Kennicutt, R. C., & Evans, N. J. 2012, *ARA&A*, 50, 531
- Kennicutt, Jr., R. C., Edgar, B. K., & Hodge, P. W. 1989, *ApJ*, 337, 761
- Klein, U., Weiland, H., & Brinks, E. 1991, *A&A*, 246, 323
- Klein, U., Wielebinski, R., & Thuan, T. X. 1984, *A&A*, 141, 241
- Kobulnicky, H. A., & Johnson, K. E. 1999, *ApJ*, 527, 154
- Kotulla, R., Fritze, U., Weibacher, P., & Anders, P. 2009, *MNRAS*, 396, 462
- Krumholz, M. R., Cunningham, A. J., Klein, R. I., & McKee, C. F. 2010, *ApJ*, 713, 1120
- Lacki, B. C., Thompson, T. A., & Quataert, E. 2010, *ApJ*, 717, 1
- Leitherer, C. 1990, *ApJS*, 73, 1
- Leitherer, C., Schaerer, D., Goldader, J. D., González Delgado, R. M., Robert, C., Kune, D. F., de Mello, D. F., Devost, D., & Heckman, T. M. 1999, *ApJS*, 123, 3
- Leroy, A. K., Bigiel, F., de Blok, W. J. G., Boissier, S., Bolatto, A., Brinks, E., Madore, B., Muñoz-Mateos, J.-C., Murphy, E., Sandstrom, K., Schrubba, A., & Walter, F. 2012, *AJ*, 144, 3
- Lotz, J. M., Jonsson, P., Cox, T. J., Croton, D., Primack, J. R., Somerville, R. S., & Stewart, K. 2011, *ApJ*, 742, 103
- Madden, S. C., Galliano, F., Jones, A. P., & Sauvage, M. 2006, *A&A*, 446, 877
- Malumuth, E. M., & Heap, S. R. 1994, *AJ*, 107, 1054
- Meurer, G. R., Heckman, T. M., Lehnert, M. D., Leitherer, C., & Lowenthal, J. 1997, *AJ*, 114, 54
- Mezger, P. G., Schraml, J., & Terzian, Y. 1967, *ApJ*, 150, 807
- Mills, B. Y., Turtle, A. J., & Watkinson, A. 1978, *MNRAS*, 185, 263
- Murphy, E. J., Condon, J. J., Schinnerer, E., Kennicutt, R. C., Calzetti, D., Armus, L., Helou, G., Turner, J. L., Aniano, G., Beirão, P., Bolatto, A. D., Brandl, B. R., Croxall, K. V., Dale, D. A., Donovan Meyer, J. L., Draine, B. T., Engelbracht, C., Hunt, L. K., Hao, C.-N., Koda, J., Roussel, H., Skibba, R., & Smith, J.-D. T. 2011, *ApJ*, 737, 67
- Murray, N., Quataert, E., & Thompson, T. A. 2010, *ApJ*, 709, 191
- Niklas, S., Klein, U., & Wielebinski, R. 1997, *A&A*, 322, 19
- Oey, M. S., & Clarke, C. J. 1998, *AJ*, 115, 1543
- Ostriker, E. C., & Shetty, R. 2011, *ApJ*, 731, 41
- Perley, R. A., & Butler, B. J. 2012, *ArXiv e-prints*
- Plante, S., & Sauvage, M. 2002, *AJ*, 124, 1995
- Pleuss, P. O., Heller, C. H., & Fricke, K. J. 2000, *A&A*, 361, 913
- Reines, A. E., & Deller, A. T. 2012, *ApJ*, 750, L24
- Reines, A. E., Johnson, K. E., & Goss, W. M. 2008a, *AJ*, 135, 2222
- Reines, A. E., Johnson, K. E., & Hunt, L. K. 2008b, *AJ*, 136, 1415
- Reines, A. E., Nidever, D. L., Whelan, D. G., & Johnson, K. E. 2010, *ApJ*, 708, 26
- Reines, A. E., Sivakoff, G. R., Johnson, K. E., & Brogan, C. L. 2011, *Nature*, 470, 66
- Relaño, M., Kennicutt, Jr., R. C., Eldridge, J. J., Lee, J. C., & Verley, S. 2012, *MNRAS*, 423, 2933
- Sargent, W. L. W., & Searle, L. 1970, *ApJ*, 162, L155+
- Schlafly, E. F., & Finkbeiner, D. P. 2011, *ApJ*, 737, 103
- Schlegel, D. J., Finkbeiner, D. P., & Davis, M. 1998, *ApJ*, 500, 525
- Scoville, N. Z., Polletta, M., Ewald, S., Stolovy, S. R., Thompson, R., & Rieke, M. 2001, *AJ*, 122, 3017
- Searle, L., & Sargent, W. L. W. 1972, *ApJ*, 173, 25
- Sramek, R. A., & Weedman, D. W. 1986, *ApJ*, 302, 640
- Storey, P. J., & Hummer, D. G. 1995, *MNRAS*, 272, 41
- Thompson, T. A., Quataert, E., & Murray, N. 2005, *ApJ*, 630, 167
- Thuan, T. X., Sauvage, M., & Madden, S. 1999, *ApJ*, 516, 783
- Tully, R. B., & Fisher, J. R. 1988, *Catalog of Nearby Galaxies*, ed. Tully, R. B. & Fisher, J. R.
- Ulvestad, J., Beresford, R., Sowsinski, K., & Broadwell, C. 1998, *VLA-Pie Town Link Test Report*, VLA Test Memo 217, NRAO
- Vacca, W. D. 1994, *ApJ*, 421, 140
- Vacca, W. D., Garmany, C. D., & Shull, J. M. 1996, *ApJ*, 460, 914
- van Zee, L., Skillman, E. D., & Salzer, J. J. 1998, *AJ*, 116, 1186
- Vanzi, L., Cresci, G., Telles, E., & Melnick, J. 2008, *A&A*, 486, 393
- Vanzi, L., Rieke, G. H., Martin, C. L., & Shields, J. C. 1996, *ApJ*, 466, 150
- Walborn, N. R. 1991, in *IAU Symposium*, Vol. 148, *The Magellanic Clouds*, ed. R. Haynes & D. Milne, 145
- Walsh, J. R., & Roy, J. 1993, *MNRAS*, 262, 27
- Wang, B., & Heckman, T. M. 1996, *ApJ*, 457, 645
- Weidner, C., Bonnell, I. A., & Zinnecker, H. 2010, *ApJ*, 724, 1503
- Wynn-Williams, C. G., & Becklin, E. E. 1986, *ApJ*, 308, 620
- Youngblood, A. J., & Hunter, D. A. 1999, *ApJ*, 519, 55

TABLE 1
SUMMARY OF VLA OBSERVATIONS

Wavelength cm	Frequency GHz	Array Config.	Date Observed	Program Code	Flux Calibrator	Phase Calibrator
6.2	4.86	A	1999 August 23	AT227	1331+305	0532+075
6.2	4.86	A+PT	2006 March 14, 20-21	AJ324	1331+305	0552+032
6.2	4.86	A	2006 March 26-27	AJ324	1331+305	0552+032
3.5	8.46	A	1999 August 23	AT227	1331+305	0532+075
3.5	8.46	A	2002 February 15-16	AJ286	1331+305	0552+032
1.3	22.46	A	1999 August 23	AT227	1331+305	0552+032
1.3	22.46	A+PT	2002 January 30	AT272	0542+498	0552+032
1.3	22.46	B	2006 August 20, 25-28	AJ324	1331+305	0552+032

TABLE 2
SUMMARY OF RADIO CONTINUUM IMAGE PROPERTIES

Wavelength cm	Frequency GHz	Robust	UV range k λ	Beam "	PA °	Noise μ Jy beam $^{-1}$
Matched u - v coverage images						
6.2	4.86	0	11.2 – 1000	0.41×0.24	21.6	10.7
3.5	8.46	0	11.2 – 1000	0.41×0.24	21.6	23.7
1.3	22.46	0	11.2 – 1000	0.41×0.24	21.6	38.3
High resolution image						
1.3	22.46	0	11.2 – 5500	0.14×0.12	28.2	24.0

TABLE 3
HST FLUX DENSITIES FOR OPTICAL CLUSTERS

Name	10^{-18} f_{F555W} erg s $^{-1}$ cm $^{-2}$ Å $^{-1}$	10^{-18} f_{F658N} erg s $^{-1}$ cm $^{-2}$ Å $^{-1}$	10^{-18} f_{F814W} erg s $^{-1}$ cm $^{-2}$ Å $^{-1}$
SSC-N	163	751	65
SSC-S	60	87	48

NOTE. — The errors on the flux densities in all filters is 10%.

TABLE 4
RADIO CONTINUUM SPECTRUM OF THE CENTRAL COMPACT REGION OF II Zw 40

Wavelength cm	Frequency GHz	Flux Density ^a mJy	Error ^b mJy	Total Flux Density ^c mJy	Missing Flux %
1.3	22.46	7.0	1.4	17.9	-61.0
3.5	8.46	8.0	1.6	19.6	-58.9
6.2	4.86	10.1	2.0	20.6	-51.0

^a Flux densities derived from matched u - v coverage images. See § 2.1 and 3.1.1 for details.

^b The errors are estimated to be 20% based on typical VLA absolute flux density calibration uncertainties.

^c Estimated using model from Klein et al. (1991)

TABLE 5
1.3 CM RADIO CONTINUUM SOURCE FLUX DENSITIES

Name	RA J2000	Dec J2000	Compact (C) or Diffuse (D)	Peak Flux mJy beam ⁻¹	Flux Density ^a mJy
A	5 55 42.589	3 23 31.86	D	0.18	0.08 ± 0.04
B	5 55 42.596	3 23 31.41	D	0.15	0.05 ± 0.04
C	5 55 42.603	3 23 31.73	D	0.17	0.04 ± 0.04
D ^b	5 55 42.609	3 23 31.98	C	0.42	0.67 ± 0.03
E	5 55 42.614	3 23 32.35	C	0.15	0.06 ± 0.05
F	5 55 42.614	3 23 31.67	D	0.15	0.03 ± 0.04
G ^b	5 55 42.616	3 23 32.02	C	0.39	0.36 ± 0.03
H	5 55 42.623	3 23 32.12	C	0.33	0.34 ± 0.03
I	5 55 42.626	3 23 32.26	C	0.15	0.04 ± 0.06
J	5 55 42.632	3 23 31.82	D	0.19	0.10 ± 0.03
K	5 55 42.642	3 23 32.05	C	0.27	0.16 ± 0.04
Combined Regions ^c					
DG	0.87 ± 0.03
DGH	1.24 ± 0.03
Entire Region ^d	4.42 ± 0.03

^a Since these sources are compared to each other and not to measurements at other wavelengths, the errors on the flux densities are the statistical errors and do not take into account the 20% uncertainty in the photometry.

^b The individual fluxes for sources D and G are very uncertain because we barely resolve them as two separate sources.

^c The properties of the combined regions were determined using regions including all the named sources rather than simply adding together the values for the individual sources.

^d The flux density determined here is lower than the flux density determined in Table 4 because here we are using an aperture defined by the 3σ contour of the high resolution image and there we used an aperture corresponding to the 3σ contour in the lower resolution, matched beam image.

TABLE 6
PROPERTIES OF THE 1.3 CM RADIO CONTINUUM SOURCES

Name	N_{ion} 10^{51} s^{-1}	N_{ostars}	$M_{cluster}$ $10^4 M_{\odot}$	SFR $M_{\odot} \text{ yr}^{-1}$
A	0.8	80	1.6	...
B	0.5	50	1.0	...
C	0.5	50	0.9	...
D	7.1	710	14.2	...
E	0.7	70	1.3	...
F	0.3	30	0.6	...
G	3.8	380	7.6	...
H	3.6	360	7.1	...
I	0.4	40	0.9	...
J	1.1	110	2.1	...
K	1.7	170	3.4	...
Combined Regions ^a				
DG	9.2	920	...	0.07
DGH	13.0	1300	...	0.09
Entire Region	46.6	4660	...	0.34

^a The properties of the combined regions were determined using regions including all the named sources rather than simply adding together the values for the individual sources.

TABLE 7
PROPERTIES OF THE OPTICAL CLUSTERS

Name	H α flux 10^{-15} erg s $^{-1}$ cm $^{-2}$	H α flux (extinction corrected) ^a 10^{-15} erg s $^{-1}$ cm $^{-2}$	N_{ion} 10^{51} s $^{-1}$	N_{Ostars}	Age ^b Myr	Mass ^c $10^4 M_{\odot}$
SSC-N	50.1 ± 6.1	182.0 ± 22.2	$\gtrsim 2.03$	$\gtrsim 200$	$\lesssim 5.0$	9.0
SSC-S	2.5 ± 1.1	9.3 ± 4.1	0.10	10	$9.4_{-1.0}^{+1.4}$	16.0

^a Corrected for foreground Galactic extinction using an $E(B-V)=0.57$.

^b Derived from H α equivalent widths.

^c Derived using broadband fluxes. See Table 3 for values.

TABLE 8
HST FLUX DENSITIES FOR RADIO SOURCES

Name	f_{F555W} 10^{-18} erg s $^{-1}$ cm $^{-2}$ \AA^{-1}	f_{F658N} 10^{-18} erg s $^{-1}$ cm $^{-2}$ \AA^{-1}	f_{F814W} 10^{-18} erg s $^{-1}$ cm $^{-2}$ \AA^{-1}
A	5.28 ± 0.22	36.70 ± 1.11	1.36 ± 0.06
B	2.15 ± 0.13	13.40 ± 1.17	0.35 ± 0.04
C	9.85 ± 0.82	88.70 ± 7.96	2.25 ± 0.19
D ^a	67.30 ± 0.30	493.00 ± 2.51	17.20 ± 0.09
E	1.19 ± 0.07	7.52 ± 0.79	0.41 ± 0.05
F	1.34 ± 1.16	25.50 ± 8.27	1.79 ± 0.23
G ^a	82.10 ± 0.50	296.00 ± 3.74	35.30 ± 0.14
H	40.20 ± 0.24	246.00 ± 1.85	14.00 ± 0.08
I	1.99 ± 0.17	11.70 ± 2.50	0.87 ± 0.06
J	17.50 ± 0.24	118.00 ± 2.13	3.77 ± 0.08
K	15.00 ± 0.38	133.00 ± 5.00	2.97 ± 0.16
Combined Regions ^b			
DG	116.00 ± 0.41	599.00 ± 3.21	43.10 ± 0.14
DGH	151.00 ± 0.33	849.00 ± 2.16	56.00 ± 0.13
Entire Region	678.00 ± 0.64	4640.00 ± 4.01	197.00 ± 0.24

^a The individual fluxes for sources D and G are very uncertain because we barely resolve them as two separate sources.

^b The properties of the combined regions were determined using regions including all the named sources rather than simply adding together the values for the individual sources.

TABLE 9
EXTINCTION VALUES DERIVED FOR RADIO CONTINUUM SOURCES

Name	Est. F658N Continuum ^a 10^{-16} erg s $^{-1}$ cm $^{-2}$ \AA^{-1}	$f_{H\alpha}$ ^b 10^{-14} erg s $^{-1}$ cm $^{-2}$	$f_{H\alpha,c}$ ^c 10^{-14} erg s $^{-1}$ cm $^{-2}$	$f_{H\alpha,est}$ ^d 10^{-14} erg s $^{-1}$ cm $^{-2}$	$A_{H\alpha}$ ^e mag
A	0.035 ± 0.009	0.26 ± 0.01	0.94 ± 0.06	7 ± 4	2.22 ± 0.30
B	0.014 ± 0.005	0.09 ± 0.01	0.34 ± 0.04	5 ± 4	2.83 ± 0.45
C	0.065 ± 0.032	0.64 ± 0.07	2.33 ± 0.26	4 ± 4	0.61 ± 0.53
D	0.450 ± 0.012	3.49 ± 0.02	12.70 ± 0.55	64 ± 8	1.75 ± 0.08
E	0.008 ± 0.003	0.05 ± 0.01	0.19 ± 0.03	6 ± 5	3.76 ± 0.47
F	0.015 ± 0.045	0.19 ± 0.07	0.68 ± 0.27	3 ± 4	1.57 ± 0.87
G	0.612 ± 0.019	1.83 ± 0.03	6.66 ± 0.31	34 ± 5	1.77 ± 0.09
H	0.286 ± 0.009	1.70 ± 0.02	6.16 ± 0.27	32 ± 5	1.79 ± 0.10
I	0.015 ± 0.007	0.08 ± 0.02	0.29 ± 0.07	4 ± 6	2.82 ± 0.87
J	0.114 ± 0.009	0.83 ± 0.02	3.01 ± 0.15	10 ± 3	1.26 ± 0.19
K	0.096 ± 0.015	0.96 ± 0.04	3.48 ± 0.21	15 ± 4	1.60 ± 0.16
Combined Regions					
DG	0.833 ± 0.016	4.02 ± 0.03	14.60 ± 0.64	82 ± 10	1.88 ± 0.08
DGH	1.090 ± 0.013	5.77 ± 0.02	21.00 ± 0.91	117 ± 15	1.86 ± 0.08
Entire Region	4.640 ± 0.025	32.60 ± 0.04	118.00 ± 5.11	417 ± 52	1.37 ± 0.08

^a Continuum flux density in the F658N filter estimated by interpolating between the individual source flux densities in the F555W and F814W filters. See Section 3.2 for further details.

^b Estimated optical H α flux determined by subtracting the estimated continuum flux density in the F658N filter from the total flux density in the F658N filter and then multiplying the result by the filter width (see Section 3.2 for further details).

^c Estimated optical H α flux corrected for foreground Galactic extinction as described in Section 4.2.1.

^d H α flux predicted from the radio data and Equation 7.

^e Extinction at the wavelength of H α .